

1 **Title**

2

3 Senescent fibroblasts in the tumor stroma rewire lung cancer metabolism and plasticity

4

5 **Authors**

6

7 Jin Young Lee^{1,2}, Nabora Reyes^{1,2}, Sang-Ho Woo^{1,2}, Sakshi Goel³, Fia Stratton³,
8 Chaoyuan Kuang³, Aaron S. Mansfield⁴, Lindsay M. LaFave³, and Tien Peng^{1,2,5*}

9

10

11 ¹Department of Medicine, Division of Pulmonary, Critical Care, Allergy and Sleep
12 Medicine

13 ²Bakar Aging Research Institute

14 University of California San Francisco, San Francisco, CA 94143

15

16 ³Albert Einstein Cancer Center

17 Albert Einstein College of Medicine, Bronx, NY 10461

18

19 ⁴Department of Oncology, Division of Medical Oncology

20 Mayo Clinic, Rochester, MN 55905

21

22 ⁵Lead contact

23

24

25

26

27

28

29

30

31

32

33

34

35

36

37 *Address correspondence to:

38 Tien Peng, M.D.

39 University of California, San Francisco

40 513 Parnassus Ave.

41 HSE Building, Room 1312

42 San Francisco, CA 94143

43 Email: tien.peng@ucsf.edu

1 **Summary**

2 Senescence has been demonstrated to either inhibit or promote tumorigenesis.
3 Resolving this paradox requires spatial mapping and functional characterization of
4 senescent cells in the native tumor niche. Here, we identified senescent $p16^{Ink4a+}$
5 cancer-associated fibroblasts with a secretory phenotype that promotes fatty acid
6 uptake and utilization by aggressive lung adenocarcinoma driven by Kras and p53
7 mutations. Furthermore, rewiring of lung cancer metabolism by $p16^{Ink4a+}$ cancer-
8 associated fibroblasts also altered tumor cell identity to a highly plastic/dedifferentiated
9 state associated with progression in murine and human LUAD. Our *ex vivo* senolytic
10 screening platform identified XL888, a HSP90 inhibitor, that cleared $p16^{Ink4a+}$ cancer-
11 associated fibroblasts *in vivo*. XL888 administration after establishment of advanced
12 lung adenocarcinoma significantly reduced tumor burden concurrent with the loss of
13 plastic tumor cells. Our study identified a druggable component of the tumor stroma that
14 fulfills the metabolic requirement of tumor cells to acquire a more aggressive phenotype.

15

16

17

18

19

20

21

22

23

1 **Introduction**

2 Senescence presents a paradox for how multicellular organisms maintain proliferative
3 homeostasis over their lifespan, as this age-related cellular process has been shown to
4 either attenuate or promote tumorigenesis¹. On one hand, the induction of cell cycle
5 arrest driven by known tumor suppressors would support senescence's role as a crucial
6 checkpoint against malignant transformation. However, Judith Campisi demonstrated in
7 2001 that senescent human lung fibroblasts promoted tumor growth when co-cultured
8 together *in vitro*, and this phenomenon is driven by secreted factors from senescent
9 fibroblasts². While the ability of senescent fibroblasts to drive tumorigenesis has been
10 replicated over time *in vitro*, it is not clear if this recapitulates a functional mechanism of
11 tumor progression *in vivo*. The challenge is to spatially resolve the identity of senescent
12 cells in the tumor niche and characterize their direct interaction with tumors *in vivo*.

13
14 *KRAS* and *TP53* are two of the most prevalent mutations found in lung adenocarcinoma
15 (LUAD), the occurrence of which also correlates with advanced staging and shorter
16 survival. Genetic mouse model combining *Kras*G12D mutation (K) with p53 deletion (P)
17 produces a more aggressive LUAD that is relatively resistant to standard chemotherapy
18 when compared to either mutations alone³. The induction of KP also generates more
19 intratumoral heterogeneity when compared with K alone, as single cell studies have
20 highlighted unique tumor subsets that arise from advanced KP-LUAD^{4,5}. These
21 emergent tumor subsets, arising from mature alveolar type 2 cells (AT2), are marked by
22 gene regulatory programs characterized by a dedifferentiated or "plastic" cell state that
23 recapitulates the lineage of foregut endoderm from which AT2 originates. Also of note is

1 that the dedifferentiated tumors share markers with recently identified transitional cell
2 states arising from AT2 to alveolar type 1 (AT1) differentiation during injury repair⁶⁻⁸,
3 which is modified by stromal factors in the AT2 niche⁶. These data suggest that
4 reorganization of the tumor stroma could play a vital role in the emergence of LUAD
5 subsets that drive disease progression.

6
7 Leveraging our ultrasensitive reporter of $p16^{Ink4a}$, we previously demonstrated that
8 senescent fibroblasts in healthy tissues promote epithelial stem cell regeneration after
9 injury⁹. In this study, we set out to determine whether cancer co-opts the regenerative
10 properties of senescent cells in a transformed stem cell niche. By spatial mapping of
11 $p16^{Ink4a+}$ cells in the tumor stroma and characterizing their interactions with LUAD, we
12 aim to resolve the senescence paradox by deconstructing the tumor-intrinsic and tumor-
13 extrinsic role of senescence in cancer.

14 **Results**

15 **Emergence of $p16^{Ink4a+}$ cancer-associated fibroblasts in the tumor stroma in** 16 **aggressive LUAD**

17
18 To characterize $p16^{Ink4a+}$ cells during malignant transformation *in vivo*, we crossed our
19 INK4A H2B-GFP Reporter-In-Tandem (INKBRITE) mouse⁹ with an autochthonous
20 model of aggressive LUAD ($Kras^{G12D/+}; Trp53^{fl/fl}; Rosa26^{tdTomato/+}$)³. This combined
21 reporter/LUAD model (hereafter referred to as KPTI) enabled simultaneous tracing of
22 tumor (tdTomato+) and $p16^{Ink4a+}$ cells (nuclear GFP+) after adenoviral-mediated Cre
23 recombination (**Fig. 1A**). We observed extensive infiltration of GFP+ cells within the

1 tumor stroma around 8-10 weeks following the induction of LUAD in the KPTI mice *via*
2 intratracheal adenoviral Cre delivery (**Fig. 1B**). Immunohistochemistry (IHC) analysis of
3 the tumor demonstrated that many of the GFP+ cells within the tumor are ACTA2+,
4 which is a cancer-associated fibroblast (CAF) marker associated with myfibroblastic
5 differentiation (myCAF), whereas GFP+ cell on the tumor margin co-localize with the
6 inflammatory CAF(iCAF)/adventitial fibroblast marker, PI16(peptidase inhibitor16) (**Fig.**
7 **1C**)^{10,11}. We performed single cell transcriptome analysis of sorted GFP+ ($p16^{Ink4a+}$)
8 and GFP- ($p16^{Ink4a-}$) fibroblasts from KPTI lungs, then merged this data with our
9 reference dataset of fibroblast populations from the normal lung. We utilized previously
10 published gene signature of CAF populations to annotate our CAF populations^{10,11},
11 which demonstrated that the majority of $p16^{Ink4a+}$ fibroblasts in KPTI lungs are myCAFs,
12 which are absent in the normal lung (**Fig. 1D, Supplemental Fig. 1A-C, Supplemental**
13 **Table 1,2**). In contrast, the iCAF population mostly clustered with adventitial fibroblasts
14 in the normal lung (hereafter referred to as iCAF/adventitial) (**Fig. 1D, Supplemental**
15 **Fig. 1A-C**). Flow cytometry of myCAF-specific surface marker, ITGA1, confirmed that
16 the majority of myCAFs were $p16^{Ink4a+}$ (**Supplemental Fig. 1D,E**), and transcript
17 analysis of $p16^{Ink4a+}$ fibroblasts isolated from KPTI lungs demonstrated significant
18 enrichment for myCAF markers (**Supplemental Fig. 1F**). Isolated $p16^{Ink4a+}$ CAFs were
19 highly enriched for characteristics associated with both senescent cells and
20 myfibroblasts^{12,13}, including F-actin aggregation, cell size enlargement, polynucleation,
21 DNA damage (γ -H2AX foci), proliferative arrest, and β -galactosidase activity (**Fig. 1E,**
22 **Supplemental Fig. 1G-I**).

1 To spatially resolve the gene signature associated with CAFs^{10,11} and recently
2 identified LUAD subsets^{4,5}, we conducted spatial analysis of 429 unique mRNA probes
3 on section from a KPTI lung (12 weeks from induction) using the Xenium platform (**Fig.**
4 **1F₁, Supplemental Table 3**). Probes for *tdtomato* and *GFP* enabled visualization of
5 tumor and *p16^{Ink4a}* cells respectively (**Fig. 1F₂₋₄**). Overlaying spatial transcript
6 coordinates (colored circles) with cellular segmentation, we could identify tumor stroma
7 free of tumor transcripts (*Lamp3*) that were occupied by transcripts of *p16^{Ink4a}* myCAFs
8 (*GFP*, *postn*, *acta2*) (**Fig. 1F₃**). In contrast, transcripts for *p16^{Ink4a}* iCAFs/adventitial
9 fibroblasts (*GFP*, *ccl7*, *tnfaip6*) were most localized on tumor margin (**Fig. 1F₄**). This is
10 confirmed by gene transcript density mapping demonstrating infiltration of myCAF
11 markers within the tumor and iCAF/adventitial fibroblast markers on the tumor margins
12 (**Fig. 1G**).

14 ***p16^{Ink4a}* CAFs form a spatially segregated niche with an aggressive LUAD subset**

15 We integrated single cell spatial data generated by Xenium into the Seurat workflow for
16 clustering using uniform manifold approximation and projection (UMAP), followed by cell
17 annotation using gene signature enrichment (UCell)¹⁴. We were able to identify clusters
18 of previously identified CAFs^{10,11} along with LUAD subsets that ranged from cells with
19 mature alveolar type 2 (AT2) markers to a dedifferentiated/plastic cell state called “high-
20 plasticity cell state” (HPCS) identified in murine lungs with KRAS mutation⁵ (**Fig. 2A,**
21 **Supplemental Fig. 2A, Supplemental Table 4**). The tumor clusters generated from the
22 spatial data is comparable to the single cell analysis of sorted tdTomato+ cells from
23 KPTI lungs (**Supplemental Fig. 2B-D, Supplemental Table 5**). Spatial analysis

1 demonstrated that HPCS cells occupy distinct regions within the tumor, and are
2 characterized by the induction of genes associated with alveolar transitional states
3 emerging with injury (e.g. *Cldn4*, *Krt7*, *S100a14*)^{6,7} concurrent with the loss of canonical
4 AT2 gene expression (e.g. *Lamp3*, *Sftpc*, *Hc*) (**Fig. 2B, Supplemental Fig. 2E**).
5 Mapping the distinct clusters generated by Seurat back onto the tumor section, we
6 observed spatial segregation of HPCS cells within the tumor that are infiltrated by
7 *p16^{Ink4a}*+ myCAFs (**Fig. 2C,D**), and these areas of HPCS correlated with higher
8 histologic tumor grades (**Fig. 2E**). Cell-to-cell distance analysis of tumor sections
9 demonstrated that *p16^{Ink4a}*+ myCAFs (GFP+/ACTA2+, green arrows) are located closer
10 to HPCS (S100A14+/tdTomato+, yellow arrows) than non-HPCS (S100A14-/tdTomato-)
11 cells within the tumor (**Fig. 2F,G**). These results demonstrate that *p16^{Ink4a}*+ myCAFs are
12 preferentially localized adjacent to an aggressive LUAD subset, suggesting a functional
13 interaction between the tumor stroma and specific tumor subsets that is driving tumor
14 heterogeneity and progression.

15

16 ***p16^{Ink4a}*+ CAFs promote the emergence of aggressive LUAD subset**

17 To explore the functional role of *p16^{Ink4a}*+ CAFs in LUAD progression, we established a
18 3D organoid co-culture system on an air-liquid interface using freshly sorted fibroblasts
19 (GFP+ vs. GFP-) and tumor cells (tdTomato+) from KPTI lungs (**Fig. 3A**). Coculture of
20 *p16^{Ink4a}*+ CAFs with tumor significantly enhanced organoid growth (**Fig. 3B**). Single cell
21 analysis of LUAD arising in KPTI yielded surface markers for HPCS, including LY6A,
22 that enabled flow sorting (**Supplemental Fig. 2E**). Sorted LY6A+ tumor displayed
23 significantly enhanced growth (**Supplemental Fig. 3A**). Analysis of the tumor-CAF

1 organoids demonstrated that $p16^{Ink4a+}$ CAFs significantly increased LY6A⁺ tumors, which
2 is confirmed on flow analysis of the tumor organoids (**Fig. 3C,D**). Transcript analysis of
3 sorted tumor cells (tdTomato⁺) confirmed the upregulation of HPCS markers concurrent
4 with downregulation of AT2 markers in tumor organoids with $p16^{Ink4a+}$ CAFs
5 (**Supplemental Fig. 3B,C**). We performed single cell RNAseq analysis of the tumor
6 organoids with gene signature enrichment analysis for cellular annotation, which
7 confirmed the increase in HPCS subsets when cocultured with $p16^{Ink4a+}$ CAFs *in vitro*,
8 and demonstrated recapitulation of the LUAD heterogeneity subsets seen *in vivo* (**Fig.**
9 **3E,F, Supplemental Fig. 3D, Supplemental Table 6**). Finally, adoptive transfer of
10 $p16^{Ink4a+}$ CAFs along with tdTomato⁺ LUAD into wild-type recipient lungs resulted in a
11 significant increase in tumor burden as quantified by whole-lung microCT when
12 compared to tumors transferred with $p16^{Ink4a-}$ CAFs (**Fig. 3G,H**). Mirroring the findings
13 from tumor organoids, $p16^{Ink4a+}$ CAFs increased the population of HPCS cells
14 expressing LY6A and S100A14 in the engrafted tumor (**Fig. 3I,J**). These experiments
15 demonstrated that $p16^{Ink4a+}$ CAFs are sufficient to drive the emergence of HPCS from
16 LUAD, likely through secreted factors from the senescent CAFs.

17

18 **$p16^{Ink4a+}$ CAFs secrete APOE to promote highly plastic LUAD phenotype**

19 We applied NicheNet¹⁵, an algorithm that predicts ligand-receptor interactions in single
20 cell data, to predict interactions of ligands which are highly expressed in $p16^{Ink4a+}$ CAFs
21 with cognate receptors expressed in LUAD from our single cell analysis of KPTI lungs
22 (**Fig. 4A**). Our analysis identified several ligands highly expressed in $p16^{Ink4a+}$ CAFs
23 and corresponding receptors on tumor cells. Among these ligands, APOE protein was

1 markedly upregulated in $p16^{Ink4a+}$ myCAFs (**Fig. 4B**), and *ApoE* transcript was
2 significantly enriched in $p16^{Ink4a+}$ CAFs (**Fig. 4C**). Spatial transcriptomic analysis
3 confirmed the presence of *ApoE* transcripts in $p16^{Ink4a+}$ myCAFs (**Fig. 4D**). Addition of
4 recombinant APOE protein to $p16^{Ink4a-}$ CAFs cocultured with LUAD recapitulated the
5 effects of $p16^{Ink4a+}$ CAFs in tumor organoid model, with APOE enhancing organoid
6 growth (**Fig. 4E,F**) while increasing the fraction of LY6A+ LUAD (**Fig. 4G-H**).
7 Conversely, blocking APOE binding to low density lipoprotein receptor (LDLR) through
8 the APOE mimetic peptide, COG133, attenuated the effects of $p16^{Ink4a+}$ CAFs in the
9 tumor organoids by decreasing proliferation and the emergence of HPCS cells (**Fig. 4I-**
10 **K**).

11

12 **APOE secreted by $p16^{Ink4a+}$ CAFs promote lipid uptake and utilization by HPCS**

13 APOE is a pleiotropic extracellular protein best known for its role in lipid transport¹⁶. We
14 noticed that the KPTI tumor contained areas with vacuolated cytoplasm suggestive of
15 lipid-laden cells. Oil red O and Bodipy staining confirmed lipid-laden tumor cells with
16 HPCS markers (**Fig. 5A**), and spatial transcriptomic analysis demonstrated enrichment
17 of *ApoE* and HPCS transcripts in the vacuolated regions of tumor (**Fig 5B**,
18 **Supplemental Fig. 4A**). Aggressive cancer cells rely on fatty acids as a fuel source for
19 biosynthesis and energy^{17,18}. Bodipy stain of LUAD organoid treated with APOE or
20 cocultured with $p16^{Ink4a+}$ CAFs demonstrated increase in lipid droplet formation in
21 LY6A+ tumor (**Fig. 5C, Supplemental Fig. 4B**). Addition of Bodipy-conjugated long
22 chain fatty acid (LCFA) to the tumor organoids treated with APOE demonstrated that
23 HPCS cells increased LCFA uptake (relative to non-HPCS cells) at baseline that is

1 significantly upregulated in the presence of APOE (**Fig. 5D,E**). We knocked down *ApoE*
2 expression in *p16^{Ink4a}*+ CAFs (ApoE KD) using lentiviral-shAPOE (**Supplemental Fig.**
3 **4C**), which resulted in reduced LCFA uptake in the tumor organoids cocultured with
4 ApoE KD *p16^{Ink4a}*+ CAFs (**Fig. 5F**) and reduced HPCS in the tumor organoid
5 (**Supplemental Fig. 4D**). LCFA profiling of the tumor organoids by liquid
6 chromatography-mass spectrometry demonstrated an enrichment of LCFA 18-24
7 carbons in length in both tumor co-cultured with *p16^{Ink4a}*+ CAFs and those treated with
8 APOE (**Fig. 5G, Supplemental Fig. 4E**). Inhibition of the fatty acid β -oxidation (FAO)
9 pathway (**Fig. 5H**) utilizing the CPT1 inhibitor, etomoxir, led to a significant reduction in
10 proliferation along with markedly decreased HPCS in the tumor organoid cocultured
11 with *p16^{Ink4a}*+ CAFs (**Fig. 5I-K**). These results show that the senescent tumor stroma
12 can rewire lipid metabolism of aggressive LUAD through APOE to increase tumor
13 fitness.

14

15 **Clearance of *p16^{Ink4a}*+ CAFs suppresses tumor progression**

16 Prior single cell analyses have demonstrated high similarity in transcriptomes of
17 myCAFs arising in cancer and myofibroblast/fibrotic fibroblast enriched in TGF β
18 activation in fibrotic tissues^{11,19}, which is consistent with our data when merging single
19 cell datasets of *p16^{Ink4a}*+ fibroblasts isolated from LUAD and lung fibrosis (bleomycin)
20 models (**Supplemental Fig, 5A-C, Supplemental Table 7**). We recently reported a
21 platform to screen for senolytic compounds targeting fibrotic *p16^{Ink4a}*+ fibroblasts in lung
22 fibrosis utilizing precision cut lung slice (PCLS) culture²⁰. To screen for multiple

1 senolytic compounds for efficacy against $p16^{Ink4a+}$ CAFs within the preserved tumor
2 microenvironment, we generated high-volume PCLS cultures from KPTI lungs (**Fig.**
3 **6A,B**) that enabled quantification of GFP+/GFP- fibroblast ratio by FACS after
4 compound treatment *ex vivo* (**Fig. 6C**). Our lead senolytic compound in the lung fibrosis
5 screen was XL888, a heat shock protein 90 inhibitor²⁰. In KPTI-PCLS, XL888
6 significantly reduced GFP+ fibroblast fraction after 5 days of treatment as analyzed by
7 FACS (**Fig. 6D**), which is confirmed on IHC analysis of the PCLS showing clearance of
8 $p16^{Ink4a+}$ myCAFs (GFP+/ACTA2+) within the intact tumor stroma (**Fig. 6E,F**). FACS
9 analysis of KPTI-PCLS also demonstrated that BH3 mimetics²¹ (navitoclax and ABT-
10 737) have potential efficacy in clearing $p16^{Ink4a+}$ CAFs (**Supplemental Fig. 5D**).

11 We then tested the effects of XL888 *in vivo* by treating KPTI mouse with XL888
12 after establishment of tumor 8 weeks out from induction (**Fig. 6G**). MicroCT
13 quantification of tumor volume demonstrated that XL888 significantly reduced tumor
14 burden after 3 weeks of treatment (**Fig. 6H,I**). IHC analysis confirmed the reduction in
15 $p16^{Ink4a+}$ myCAFs after XL888 treatment (**Fig. 6J,K**). Furthermore, XL888-treated KPTI
16 lungs demonstrated decreased HPCS cells in the tumors (**Fig. 6L,M**). Flow cytometry
17 analysis revealed no change in the percentage of $p16^{Ink4a+}$ immune cells
18 (GFP+/CD45+) in the XL888-treated KPTI lungs (**Supplemental Fig. 5E**). The PCLS
19 senolytic screen demonstrated that the combination of dasatinib and quercetin (D&Q)²²
20 did not have efficacy in clearing $p16^{Ink4a+}$ myCAFs (**Supplemental Fig. 5D**). D&Q did
21 not reduce $p16^{Ink4a+}$ myCAFs nor tumor burden when administered *in vivo* to KPTI
22 animals with established tumor (**Supplemental Fig. 5F-I**). These results suggested that
23 the efficacy of senolytics is context/target dependent, and demonstrated that clearance

1 of $p16^{Ink4a+}$ myCAFs with XL888 attenuated tumor progression and prevented the
2 emergence of plastic tumor subsets in an aggressive model of LUAD.

3

4 **$p16^{INK4A}$ promotes myCAF phenotype in human lung fibroblasts**

5 Analysis of previously published cell atlas of CAFs identified in patients with non-small
6 cell lung cancer (NSCLC)²³ demonstrated the enrichment of *CDKN2A* (encodes both
7 $p16^{INK4A}$ and $p14^{ARF}$ in alternative reading frames) in myCAFs that are also enriched for
8 *CTHRC1* and *POSTN*, similar to the murine myCAFs (**Supplemental Fig. 6A**). To
9 confirm the spatial localization of myCAFs in relation to tumor subsets in human LUAD,
10 we applied our spatial analysis workflow utilizing a human probe set for lung epithelial
11 and fibroblast subtypes (**Supplemental Table 8**) on a biopsy sample of LUAD with
12 *KRAS* driver mutation (G12A). Transcript identification with cell segmentation generated
13 unique clusters that were annotated using gene enrichment analysis and mapped onto
14 the slide (**Fig. 7A,B, Supplemental Fig. 6B, Supplemental Table 9**). We were able to
15 identify *CDKN2A+/APOE+* myCAFs in the tumor stroma adjacent to recently described
16 transitional/plastic cell (*KRT8+/CLDN4+*) found primarily in patients with *KRAS*-mutated
17 LUAD²⁴ (**Fig. 7B**). IHC analysis of LUAD samples confirms the presence of $p16^{INK4A}$
18 protein in the myCAFs within the tumor stroma (**Supplemental Fig. 6C**). Applying a
19 gene signature derived from single cell data of human $p16^{INK4A+}$ myCAFs in NSCLC²³ to
20 the Cancer Genome Atlas (TCGA) dataset demonstrated a significant correlation
21 between $p16^{INK4A+}$ myCAF gene signature expression level in tumor samples and
22 mortality in patients with LUAD (**Fig. 7C, Supplemental Table 10**).

1 To test the sufficiency of $p16^{INK4A}$ expression in the induction of the human
2 myCAF phenotype, we designed a dual lentiviral system (Lenti-tTS/rTTA+Lenti-TRE-
3 p16-2A-tdTomato) to overexpress (OE) $p16^{INK4A}$ in primary human fibroblasts isolated
4 from control donors in a doxycycline (dox) dependent fashion. The transduced human
5 lung fibroblasts are cocultured with human LUAD organoids generated from NSCLC
6 patients with KRAS driver mutations like our 3D CAF-tumor organoid model for KPTI
7 (**Fig. 7D**). Dox induction (p16OE) of the human CAF-tumor organoid significantly
8 enhanced tumor growth *in vitro* (**Fig. 7E,F**). Transcript analysis of fibroblasts confirmed
9 the induction of $p16^{INK4A}$ after dox treatment (**Fig. 7G**). Dox induction of $p16^{INK4A}$ in lung
10 fibroblasts induced myCAF signature gene expression in fibroblasts cocultured with
11 tumor, but not in the absence of tumor (**Fig. 7H**). This suggested that the tumor initiates
12 the myCAF program in $p16^{INK4A+}$ lung fibroblasts in a paracrine fashion, which then
13 initiates a $p16^{INK4A+}$ CAF-to-tumor signaling program to promote tumor progression.
14 Analysis of the tumor cells by flow cytometry demonstrated an increase in human plastic
15 cell marker⁵, ITGA2, as well as an increase in Bodipy-LCFA uptake in the tumor
16 cocultured with p16OE fibroblasts (**Fig. 7I,J**). Administration of human recombinant
17 APOE variants to the tumor organoids demonstrated that hAPOE2 had the largest effect
18 in promoting tumor organoid growth, which correlated with LCFA uptake in culture
19 (**Supplemental Fig. 6D-F**).

20

21 **Discussion**

22 One of the common links between Hayflicks's original description of a cell cycle arrest
23 termed "senescence"²⁵ and Campisi's seminal observation that senescent cells can

1 drive malignant transformation² is that both were studying human lung fibroblasts grown
2 in culture. The significance of whether these phenotypes of lung fibroblasts *in vitro*
3 correlate with their native function *in vivo* remains an open question. Our data
4 demonstrate that senescent lung fibroblasts arising in the tumor stroma drive tumor
5 evolution to a more dedifferentiated cellular state with altered metabolic requirement for
6 high-energy substrate. These tumor-intrinsic features correlate with the known features
7 of LUAD progression such as increased intratumoral heterogeneity^{4,5,26} and rewired
8 fatty acid metabolism^{17,18}, but we now present a model where tumor-extrinsic signals in
9 the stroma can drive these cancer hallmarks.

10 The emergence of lineage heterogeneity in LUAD would also suggest divergent
11 metabolic requirements that predicate their distinct function. Metabolic profiling of
12 different lung cancer cell lines demonstrated remarkable diversity, even when cultured
13 under standard conditions, that correlated with distinct oncogenic mutations as well as
14 therapeutic response²⁷. One of these divergent metabolic features is an increased
15 dependence on fatty acid utilization to sustain energy production and biomass synthesis
16 in certain tumor subtypes. Activation of KRAS has been demonstrated to increase both
17 fatty acid uptake and synthesis in LUAD that drives tumor proliferation^{17,28}. However, it
18 was not clear whether the tumor microenvironment is playing a role in this divergent
19 metabolic requirement for LUAD to utilize lipid as fuel, nor do we understand how lipid
20 utilization differs amongst LUAD tumor subsets with varying capacity to drive
21 progression. Our study demonstrated that senescent CAFs within the tumor stroma
22 rewire the metabolic requirement of an aggressive LUAD subset, and this metabolic

1 rewiring can drive tumor plasticity and sustain intratumoral heterogeneity as the LUAD
2 progresses to more advanced stages.

3 We have previously demonstrated that senescent fibroblasts in the lung stem cell
4 niche dynamically alter their secretory program to promote stem cell renewal during
5 acute injury⁹. Conceptualizing cancer as a nonhealing wound, our data suggests that
6 cancer coopts the adaptive properties of the senescent stroma in the lung to select for
7 tumor subsets with enhanced capacity to propagate. In this view, senescent fibroblasts
8 are neither good nor bad, but rather fulfills the specific requirement of the epithelial
9 niche (normal or malignant) to drive stem cell renewal regardless of the costs.
10 Uncovering this requirement does reveal a therapeutic opportunity to target the tumor
11 stroma using senolytics, but it should be noted that the senescent fibroblasts we
12 identified driving stem cell renewal in acute injury and cancer respectively are different
13 types of fibroblasts. The need for target specificity in selecting senolytics becomes more
14 apparent as the heterogeneity of senescent cells *in vivo* becomes increasingly
15 recognized.

16

17 **Acknowledgements**

18 We thank Parnassus Flow Cytometry Core for assistance with cell sorting for bulk and
19 single cell RNA analysis (P30DK063720). We thank Youngho Seo (Preclinical microCT
20 core) for processing of micro-computed tomography images. GEO accession number
21 for raw RNA sequencing data is listed in Methods. This work is supported by NIH grants
22 R01HL160895 and R01HL155622 and CIRM DISC0-14460 to T.P., the Tobacco-
23 Related Disease Research Program (TRDRP) postdoctoral award T33FT6395 and

1 Basic Science Research Program through the National Research Foundation of Korea
2 (NRF) funded by the Ministry of Education (2020R1A6A3A03038781) to J.L., and Nina
3 Ireland Program Award for human lung collection.

4

5 **Author Contributions**

6 J.L. and T.P conceived the experiments and wrote the manuscript. J.L., N.R., S.W.,
7 S.G., F.S. performed the experiments, collected samples, and analyzed data. C.K. and
8 A.S.M. collected human materials. L.M.L. provided input on the experiments and
9 manuscript.

10

11 **Declaration of Interests**

12 A.S.M. reports receiving support from Genentech and Janssen for manuscript
13 publication; receiving research support to institution from Novartis and Verily; receiving
14 honoraria to institution for participation on advisory boards for AbbVie, AstraZeneca,
15 Bristol Myers Squibb, Genentech, Janssen, and Takeda Oncology; serving as steering
16 committee member for Janssen and Johnson & Johnson Global Services; having
17 speaking engagements from Chugai Pharmaceutical Co, Ltd (Roche); serving as grant
18 reviewer for Rising Tide; having expert think tank participation in Triptych Health
19 Partners; serving as a moderator for IDEOlogy Health LLC (formerly Nexus Health
20 Media); having CME presentation for Intellisphere LLC (OncoLive Summit Series) and
21 Answers in CME; having presentation for Immunocore; serving on the advisory board
22 for Sanofi Genzyme; receiving honoraria to self for CME presentation for Antoni van
23 Leeuwenhoek Kanker Instituut and MJH Life Sciences (OncoLive); having presented to

1 the University of Miami International Mesothelioma Symposium; receiving travel support
 2 from Roche; serving as nonremunerated director of the Mesothelioma Applied Research
 3 Foundation and member of the Friends of Patan Hospital board of directors; and
 4 receiving study funding and article process charges from Bristol Myers Squibb.

5

6 **Methods**

7 **Key resource table**

REAGENT or RESOURCE	SOURCE	IDENTIFIER
Antibodies		
Rat anti-mouse CD45 PE-Cy7 (used at 1:200)	Thermo Fisher	Cat# 25-0451-82; RRID:AB_2734986
Rat anti-mouse CD45-BV421 (used at 1:200)	BD	Cat# BD563890; RRID: AB_2651151
Rat anti-mouse CD31-BV711 (used at 1:200)	BD	Cat# BD740680; RRID: AB_2740367
Rat anti-mouse CD31-eFluor450 (used at 1:200)	Thermo Fisher	Cat# 48-0311-82; RRID: AB_10598807
Rat anti-mouse CD326-PE (used at 1:200)	BD	Cat# BD 563477; RRID: AB_2738233
Rat anti-mouse CD326-BV421 (used at 1:200)	BD	Cat# BD563214; RRID: AB_2738073
Rat anti-mouse Ly6A/E-APC-Cy7 (used at 1:200)	BD	Cat# BD 560654; RRID: AB_1727552
Mouse anti-human CD45-APC-Cy7 (used at 1:200)	Biolegend	Cat# 304014; RRID: AB_314402
Mouse anti-human CD31-APC-Cy7 (used at 1:200)	Biolegend	Cat# 303120; RRID: AB_10640734
Mouse anti-human CD11b-APC-Cy7 (used at 1:200)	BD	Cat# BD 557754; RRID: AB_396860
Mouse anti-human CD326-PE (used at 1:200)	Biolegend	Cat# 324206; RRID: AB_756080
Mouse anti-human CD49b-APC (used at 1:200)	Biolegend	Cat# 359310; RRID: AB_2564199
Goat anti-GFP (used at 1:400)	abcam	Cat# ab6673; RRID: AB_305643

Chicken anti-GFP (used at 1:200)	abcam	Cat# ab13970; RRID: AB_300798
Rabbit anti-DsRed (used at 1:200)	Takara	Cat# 632496; RRID: AB_10015246
Goat anti-tdTomato (used at 1:500)	Sicgen	Cat# AB8181; RRID: AB_2722750
Rabbit anti-Laminin (used at 1:200)	Sigma	Cat# L9393; RRID: AB_477163)
Rabbit anti-mouse S100A14 (used at 1:200)	Proteintech	Cat# 10489-1-AP; RRID: AB_2183628
Rabbit anti-human Mouse SMA (used at 1:200)	Abcam	Cat# ab5694; RRID: AB_2223021
Goat anti-mouse PI16 (used at 1:200)	R&D systems	Cat# AF4929; RRID: AB_2299601
Goat anti-mouse SCA-1 (used at 2 µg/ml)	R&D systems	Cat# AF1226; RRID: AB_354679
Rabbit anti-APOE (used at 1:200)	Thermo Fisher	Cat# 701241; RRID: AB_2532438
Rabbit anti-E-Cadherin (used at 1:200)	Cell Signaling	Cat# 3195; RRID: AB_2291471
Rabbit anti-Phospho-Histone H2A.X (used at 1:200)	Cell Signaling	Cat# 9718; RRID: AB_2118009
Mouse anti-human p16 (used at 1:200)	Santa Cruz	Cat# sc-56330; RRID: AB_785018
Sheep anti-human FAP (used at 1:200)	R&D systems	Cat# AF3715; RRID: AB_2102369
Bacterial and virus strains		
Ad5CMVCre	Viral Vector Core, University of Iowa	N/A
Biological samples		
Normal Human Lung Tissues	UCSF Lung disease Blood and Tissue Repository	
Human Lung Adenocarcinoma tissues	Mayo clinics, Albert Eistein Cancer Center	
Chemicals, peptides, and recombinant proteins		
DMEM/F-12	Thermo Fisher	Cat# 11330032
Small Airway Epithelial Cell Growth Medium BulletKit	Lonza	Cat# CC-3118
Advanced DMEM/F12	Thermo Fisher	Cat# 12634-034
R-Spondin 1	Peprtech	Cat# 120-38
FGF 7	Peprtech	Cat# 100-19
FGF 10	Peprtech	Cat# 100-26
Noggin	Peprtech	Cat# 120-10C

A83-01	Tocris	Cat# 2939
Y-27632	Abmole	Cat# Y-27632
SB202190	Sigma	Cat# S7067
B27	Gibco	Cat# 17504-44
N-Acetylcysteine	Sigma	Cat# A9165-5g
Nicotinamide	Sigma	Cat# N0636
GlutaMax 100x	Invitrogen	Cat# 12634-034
Hepes	Invitrogen	Cat# 15630-056
Penicillin / Streptomycin	Invitrogen	Cat# 15140-122
Primocin	Invivogen	Cat# Ant-pm-1
TrypLE Select Enzyme	Thermo Fisher	Cat# 12563011
Fetal Bovine Serum, heat inactivated (FBS)	Thermo Fisher	Cat# 12676011
Antibiotic-Antimycotic (100X)	Thermo Fisher	Cat# A5955-100ML
Fluorsave	Millipore Sigma	Cat# 345789
DAPI (used at 1:1000)	Thermo Fisher	Cat# 1738176
SYTOX Blue (used at 1:1000)	Thermo Fisher	Cat# S34857
SYTOX Red (used at 1:1000)	Thermo Fisher	Cat# S34859
RBC Lysis Buffer (10x)	Thermo Fisher	Cat# NC9067514
Normal Donkey Serum	Thermo Fisher	Cat# 50413275
4% Paraformaldehyde (PFA) in PBS	Santa Cruz	Cat# sc-281692
Xylene	VWR	Cat# 89370-088
Paraffin	Thermo Fisher	Cat# 8330
OCT	VWR	Cat# 25608-930
Diva Decloaker Antigen Retrieval (10x)	Biocare Medical	Cat# DV2004MX
TritonX-100	Sigma Aldrich	Cat# X100
Tween 20	Thermo Fisher	Cat# BP337500
TrueBlack (50x)	Biotium	Cat# 23007
Collagenase type I	Thermo Fisher	Cat# 17100017
Dispase II	Thermo Fisher	Cat# 17105041
DNase I	Sigma Aldrich	Cat# DN25
Matrigel	Thermo Fisher	Cat# CB-40230A
FcR Blocking Reagent	Miltenyi Biotec	Cat# 130-092-575
Human FcR Blocking Reagent	BD	Cat# 564220
SuperScript III Reverse Transcriptase	Thermo Fisher	Cat# 18080044
RnaseOUT Rnase Inhibitor	Thermo Fisher	Cat# 100000840
Recombinant mouse APOE	abcam	Cat# ab226314
Recombinant human APOE2	Peptotech	Cat# 10780-826
Recombinant human APOE3	Peptotech	Cat# 10774-406
Recombinant human APOE4	Peptotech	Cat# 10774-424
COG133	Abcam	Cat# ab269699
Bodipy 493/503 (used at 2.5 μ M)	Invitrogen	D3922
Bodipy 500/510 C1, C12 (used at 2 μ g/ml)	Invitrogen	D3823
CellTrace Far Red (used at 1 μ M)	Invitrogen	C34572
EasySep mouse streptavidin RapidSpheres	StemCell	19860A
XL888	MedChemExpress	HY-13313
Dasatinib	MedChemExpress	HY-10181

Quercetin	MedChemExpress	HY-18085
ABT263	MedChemExpress	HY-10087
ABT737	MedChemExpress	HY-50907
Fisetin	MedChemExpress	HY-N0182
Critical commercial assays		
PicoPure RNA Isolation Kit	Applied Biosystems	Cat# KIT0204
RNeasy Kit	QIAGEN	Cat# 74106
DyNAmo Flash SYBR Green qPCR Kit	Thermo Fisher	Cat# F415L
RNase-Free DNase Set	QIAGEN	Cat# 79254
Deposited data		
Single-cell RNA-seq of mouse LUAD	This paper	GEO: GSE268478
Single-cell RNA-seq of human fibroblasts from hLUAD	Grout <i>et al.</i>	GEO: GSE183219
Experimental models: Cell lines		
Experimental models: Organisms/strains		
Mouse: <i>INKBRITE</i>	Reyes <i>et al.</i>	N/A
Mouse: <i>C57BL/6</i>	Jackson Laboratory	JAX# 000664
Mouse: <i>LSL-K-ras G12D</i>	Jackson Laboratory	JAX# 008179
Mouse: <i>p53LoxP</i>	Jackson Laboratory	JAX# 008462
Mouse: <i>Ai14</i>	Jackson Laboratory	JAX# 007914
Mouse: NOD.Cg-Prkdcscid Il2rgtm1Wjl/SzJ	Jackson Laboratory	JAX# 005557
Oligonucleotides		
Ms_ <i>Cthrc1</i> _Forward	IDT	5' CAGTTGTCCGC ACCGATCA 3'
Ms_ <i>Cthrc1</i> _Reverse	IDT	5' GGTCCTTG TAG ACACATTCCATT 3'
Ms_ <i>Acta2</i> _Forward	IDT	5' ACTCTCTTCCAG CCATCTTTCA 3'
Ms_ <i>Acta2</i> _Reverse	IDT	5' ATAGGTGGTTTC GTGGATGC 3'
Ms_ <i>Postn</i> _Forward	IDT	5' TGGTATCAAGG TGCTATCTGCG 3'
Ms_ <i>Postn</i> _Reverse	IDT	5' AATGCCAGCG TGCCATAA 3'

Ms_ <i>Tagln</i> _Forward	IDT	5' GGTGGCTCAAT TCTTGAAGGC 3'
Ms_ <i>Tagln</i> _Reverse	IDT	5' TGCTCCTGGGC TTTCTTCATA 3'
Ms_ <i>p16lnk4a</i> _Forward	IDT	5' AATCTCCGCGA GGAAAGC 3'
Ms_ <i>p16lnk4a</i> _Reverse	IDT	5' GTCTGCAGCGG ACTCCAT 3'
Ms_ <i>MyI9</i> _Forward	IDT	5' ACAGCGCCGAG GACTTTTC 3'
Ms_ <i>MyI9</i> _Reverse	IDT	5' AGACATTGGAC GTAGCCCTCT 3'
Ms_ <i>Tpm2</i> _Forward	IDT	5' GTGGCTGAGAG TAAATGTGGG 3'
Ms_ <i>Tpm2</i> _Reverse	IDT	5' TTGGTGGAAATA CTTGTCCGCT 3'
Ms_ <i>Col12a1</i> _Forward	IDT	5' AAGTTGACCCA CCTTCCGAC 3'
Ms_ <i>Col12a1</i> _Reverse	IDT	5' GGTCCACTGTT ATTCTGTAACCC 3'
Ms_ <i>ApoE</i> _Forward	IDT	5' CTGACAGGATG CCTAGCCG 3'
Ms_ <i>ApoE</i> _Reverse	IDT	5' CGCAGGTAATC CCAGAAGC 3'
Ms_ <i>Ly6a</i> _Forward	IDT	5' AGGAGGCAGCA GTTATTGTGG 3'
Ms_ <i>Ly6a</i> _Reverse	IDT	5' CGTTGACCTTA GTACCCAGGA 3'
Ms_ <i>Tigit</i> _Forward	IDT	5' TGCCTTCCTCG CTACAGG 3'
Ms_ <i>Tigit</i> _Reverse	IDT	5' TGCAGAGATGT TCCTCTTTGTAT C 3'
Ms_ <i>Nkx2-1</i> _Forward	IDT	5' CAGGACACCAT GCGGAACAGC 3'

Ms_ <i>Nkx2-1</i> _Reverse	IDT	5' GCCATGTTCTTG CTCACGTCCC 3'
Ms_ <i>Sftpc</i> _Forward	IDT	5' ATGGACATGAG TAGCAAAGAGG T 3'
Ms_ <i>Sftpc</i> _Reverse	IDT	5' CACGATGAGAA GGCGTTTGAG 3'
Ms_ <i>Gapdh</i> _Forward	IDT	5' GGCCCCTCCTG TTATTATGGGG GT 3'
Ms_ <i>Gapdh</i> _Reverse	IDT	5' CCCCAGCAAGG ACACTGAGCAA GA 3'
Hs_ <i>p16INK4a</i> _Forward	IDT	5' GTCGGGTAGAG GAGGTGCG 3'
Hs_ <i>p16INK4a</i> _Reverse	IDT	5' CATGACCTGGA TCGGCCTC 3'
Hs_ <i>p21</i> _Forward	IDT	5' TTGTACCCTTGT GCCTCGCT 3'
Hs_ <i>p21</i> _Reverse	IDT	5' CGTTTGGAGTG GTAGAAATCTGT C 3'
Hs_ <i>CTHRC1</i> _Forward	IDT	5' GTGGCTCACTT CGGCTAAAAT 3'
Hs_ <i>CTHRC1</i> _Reverse	IDT	5' CACTAATCCAG CACCAATTCCTT 3'
Hs_ <i>POSTN</i> _Forward	IDT	5' CTCATAGTCGTA TCAGGGGTGC 3'
Hs_ <i>POSTN</i> _Reverse	IDT	5' ACACAGTCGTTT TCTGTCCAC 3'
Hs_ <i>ACTA2</i> _Forward	IDT	5' AAAAGACAGCT ACGTGGGTGA 3'
Hs_ <i>ACTA2</i> _Reverse	IDT	5' GCCATGTTCTAT CGGGTACTTC 3'
Hs_ <i>TIMP1</i> _Forward	IDT	5' CTTCTGCAATTC CGACCTCGT 3'

Hs_ <i>TIMP1</i> _Reverse	IDT	5' ACGCTGGTATA AGGTGGTCTG 3'
Hs_ <i>APOE</i> _Forward	IDT	5' GTTGCTGGTCA CATTCTTG 3'
Hs_ <i>APOE</i> _Reverse	IDT	5' GCAGGTAATCC CAAAGCGAC 3'
Hs_ <i>RPL19</i> _Forward	IDT	5' CCCATCTTTGAT GAGCTTCC 3'
Hs_ <i>RPL19</i> _Reverse	IDT	5' TGCTCAGGCTT CAGAAGAGG 3'
Recombinant DNA		
Software and algorithms		
Fiji	N/A	https://www.imagej.net/Fiji
Imaris 8.1 (Matlab plugin Sortomato)	Bitplane	N/A
FlowJo	FLOWJO LLC	https://www.flowjo.com/
GraphPad Prism v8.3.0	GraphPad Software	https://www.graphpad.com/scientific-software/prism/
CellRanger version 3.0.2	10X Genomics	https://www.support.10xgenomics.com/single-cell-gene-expression/software/pipelines/latest/installation
R	https://www.r-project.org	N/A
RStudio	https://www.rstudio.com	N/A
Seurat R Package	https://satijalab.org/seurat/	N/A
NicheNet	Browaeys <i>et al.</i>	https://github.com/saeyslab/nichenet
SurvivalGenie	Bhakti <i>et al.</i>	https://github.com/bhasinlab/SurvivalGenie

Other		

1

2 **Animal experiments**

3 All animal studies described were approved by the IACUC at the University of

4 California, San Francisco. All genetically engineered mice were maintained on a mixed

5 or C57/BL6 background. Experiments were performed on male and female mice

6 between 8-12 weeks old. Previously published *Kras*^{LSL-G12D/+29}, *Trp53*^{flox/flox} 30,

7 *Rosa26*^{LSL-tdTomato/+} 31, Apoe knock-out (JAX002052), and INKBRITE 32 mice were used

8 in this study. In addition, we used NOD.Cg-Prkdc^{scid} Il2rg^{tm1Wjl}/SzJ (NSG mice, The

9 Jackson Laboratory, catalog #005557) in our transplantation studies. Tumors were

10 induced in KP, KPT, or KPTI mice at 8 to 12 weeks of age with 2.5x10⁷ PFU of AdCMV-

11 cre (University of Iowa) by intratracheal instillation as described previously 33. For XL888

12 treatment, KPTI mice were treated with XL888 as previously described 34. Briefly, 62.5

13 mg/kg of XL888 was delivered to mice via oral delivery 5 days a week for 3 weeks

14 starting at 8 weeks after AdCMV-cre delivery. XL888 was dissolved in 10 mM

15 hydrochloric acid with the concentration of 15.625 mg/ml. After vortexing, the dissolved

16 XL888 was delivered to the mice using oral gavage daily. For dasatinib and quercetin

17 (DQ) treatment, dasatinib (5 mg/kg) and quercetin (50 mg/kg) were administered to

18 mice via oral gavage daily for 3 weeks, starting 6 weeks after adCMV-cre delivery. The

19 compounds were dissolved in a solution consisting of 4% DMSO, 30% PEG300, 5%

20 Tween80, 61% dH2O.

1

2 **Human Lung Tissue**

3 Studies involving human tumor specimen were approved by the Mayo Clinic and Albert
4 Einstein Institutional Review Board. All subjects provided written informed consent.
5 Human lung fibroblasts were isolated from the lungs of brain-dead donors that were
6 rejected for lung transplantation. Clinical/demographic information of tissue donors are
7 listed in Supplementary Table 11.

8

9 **FACS**

10 Dissected mouse lung was tracheally perfused with a digestion cocktail of Collagenase
11 Type I (225 U/ml, Thermo Fisher Scientific), Dispase (15 U/ml, Thermo Fisher Scientific)
12 and Dnase (50 U/ml, Sigma-Aldrich) after perfusion with PBS. The lung was removed
13 from the chest and incubated in a digestion cocktail for 45 minutes at 37 °C with
14 continuous shaking. After digestion, remaining tissue chunks were finely minced with
15 blades and washed with a FACS buffer (2% FBS and 1% Penicillin-Streptomycin in
16 DMEM). The mixture was passed through a 70 µm cell strainer and resuspended in a
17 red blood cell lysis buffer, then passed through 40 µm cell strainer. Cell suspensions
18 were incubated with FcR blocker for 10 mins on the ice. After blocking, cell suspensions
19 were incubated with the appropriate conjugated antibodies in a sorting buffer for 30 min
20 at 4°C and washed with FACS buffer. Doublets and dead cells were excluded based on
21 forward and side scatter and SYTOX Red (Invitrogen, S34859), respectively.
22 The following antibodies were used for staining: CD45-PE-Cy7 (Invitrogen, 50-112-
23 9643), CD45-BV421 (BD, 563890), CD31-BV711 (BD, 740680), CD31-BV421

1 (Invitrogen, 48-0311-82), EpCAM-PE (BD, 563477), EpCAM-BV421 (BD, 563214).
2 Immune (CD45-biotin, Biolgened, 103104), epithelial (CD326-biotin, Biolegend, 118204)
3 and endothelial (CD31-Biotin, Biolegend, 102404) cells are removed with EasySep
4 mouse streptavidin RapidSpheres (StemCell, 19860A), when applicable. FACS was
5 performed on a BD FACS Aria using FACSDiva Software. CD45- CD31- EpCAM+
6 tdTomato+ cells were sorted for LUAD cells and CD45- CD31- EpCAM- cells were
7 sorted for fibroblasts, the GFP- and GFP+ fibroblasts were further separated and were
8 sorted into FACS buffer. Analysis was performed using FlowJo software.
9 For the human lung, a distal piece (~10 cm³) was dissected from the whole lung and
10 washed with HBSS X 4 times in 15 min. The piece of lung was further diced with razor
11 blades and was added into the digestion cocktail of Collagenase Type I (225 U/ml,
12 Thermo Fisher), Dispase (15 U/ml, Thermo Fisher) and Dnase (100 U/ml, Sigma). The
13 mixture was incubated for 2 h at 37°C and vortexed intermittently. The mixture was then
14 liquefied with a blender and passed through 4X4 gauze, a 100 mm and a 70 mm cell
15 strainer. The mixture was resuspended in RBC lysis buffer, before passing through a 40
16 mm cell strainer. The cell suspensions were incubated with the antibodies in the FACS
17 buffer for 30 min at 4°C and washed with the FACS buffer. The following antibodies
18 were used: CD45-APC-Cy7 (BioLegend, 304014), CD31-APC-Cy7 (BioLegend,
19 303120), CD11b-APC-Cy7 (BD Biosciences, 557754), EpCAM-PE (BioLegend,
20 324206). DAPI (0.2 mg/ml) was used to exclude dead cells. Single cells were selected
21 and CD45- CD11b- CD31- EpCAM- cells were sorted for fibroblasts. Cells were sorted
22 into FACS buffer. FACS analysis was performed by FACSDiva (BD).
23

1 **Single-cell RNA sequencing and analysis**

2 Single cell sequencing was performed on a 10X Chromium instrument (10X Genomics)
3 at the Institute of Human Genetics (UCSF, San Francisco, CA). Briefly, live mouse lung
4 cells were sorted and resuspended in 50 μ l PBS with 0.04% BSA at 1,000 cells/ μ l and
5 loaded onto a single lane into the Chromium Controller to produce gel bead-in
6 emulsions (GEMs). GEMs underwent reverse transcription for RNA barcoding and
7 cDNA amplification. The library was prepped with the Chromium Single Cell 3' Reagent
8 Version 3 kit. The samples were sequenced using the HiSeq2500 (Illumina) in Rapid
9 Run Mode. We used the Seurat R package along with a gene-barcode matrix provided
10 by Cell Ranger for downstream analysis. Following the standard workflow of Seurat, we
11 generated Seurat objects after using ScaleData, RunPCA, RunUMAP. For human
12 scRNA-seq data, we used processed scRNA-seq data from human LUAD fibroblasts
13 from GSE183219. After generating subsets of lung fibroblasts, violin plots and density
14 plots were generated.

15

16 **Xenium sample preparation**

17 5 μ m FFPE tissue sections from KPTI mouse lung tissues were placed onto a Xenium
18 slide, followed by deparaffinization and permeabilization to make the mRNA detectable.
19 The Xenium platform from 10X Genomics was used according to the manufacturer's
20 recommendations and as previously reported³⁵. The Xenium output files were
21 transferred for downstream analysis using the Xenium explorer.

22

23 **Post-Xenium histology**

1 After running Xenium platform, H&E staining followed the manufacturer's protocol
2 (CG000160). Post-Xenium H&E images were registered to Xenium data using QuPath
3 and Xenium explorer.

4

5 **Spatial cluster generation and mapping from Xenium**

6 We employed the Seurat vignette (<https://satijalab.org/seurat/reference/readxenium>) to
7 load and analyze the Xenium data with Seurat version 5. For normalization, we applied
8 SCTransform method, followed by standard dimensionality reduction and clustering.
9 The clustering results were visualized in UMAP space. Subsequently, we annotated
10 each cluster according to their gene expressions. The annotated clusters were imported
11 into the Xenium explorer to map their spatial locations.

12

13 **Histologic grading of mouse tumors**

14 Quantification of mouse lung tumor grade was performed by trained pathology
15 technician who was blinded to sample ID. The quantification was based on parameters
16 established by the previously described Aiforia platform that used automated deep
17 neural network trained to classify NSCLC tumor grades (1-4) based on NSCLC_v25
18 algorithm⁴.

19

20 **Tumor transplantation experiment**

21 8 weeks old recipient mice were injured by injecting 1-1.5U/kg bleomycin intratracheally
22 3 days before transplantation. Tumor cells and fibroblasts were obtained from LUAD-
23 induced KPTI mice by FACS as detailed in section "FACS". A mixture of 20,000

1 fibroblasts and 100,000 tumor cells or only tumor cells were resuspended in 50 μ l PBS
2 and introduced into the lungs of bleomycin-injured recipient mice intratracheally. After 4
3 weeks, lung tumor burden of recipient mice was evaluated using microCT imaging.
4 Subsequently, the mice were euthanized for lung histological analysis.

6 **3D mouse tumor organoid cultures**

7 Primary tumor organoid cultures were generated from tdTomato expressing tumor cells
8 isolated from mice bearing 2-3 months old LUAD tumors. EpCAM+ tdTomato+ tumor
9 cells were isolated by FACS and plated on Matrigel (Corning, CB-40230) as previously
10 described ³². Briefly, tumor cells and GFP- or GFP+ fibroblasts were resuspended (4-
11 5×10^3 tumor cells: $2.4-3 \times 10^4$ fibroblasts/well) in 1:1 mixture of media and Matrigel. The
12 media is comprised of small airway basal media (SABM) with selected components
13 from SAGM bullet kit (Lonza) including Insulin, Transferrin, Bovine Pituitary Extract,
14 Retinoic Acid, and human Epidermal Growth Factor. 0.1 μ g/mL cholera toxin, 5% FBS,
15 and 1% Penicillin-Streptomycin were also added. The mixture of cell suspension-
16 matrigel-media was placed in a transwell of 24 well plate and allowed to solidify at 37°C.
17 The growth media with 1 μ M of ROCK inhibitor was added to the lower well of the well
18 plate and refreshed with the media without ROCK inhibitor after 24 hr. Media was
19 refreshed every 2-3 days.

21 **Human 3D tumor organoid cultures.**

22 Human 3D tumor organoid was established as previously described ³⁶. Briefly,
23 cryopreserved human LUAD specimen was thawed in 37°C and washed with PBS to

1 remove freezing media. The tissue was placed in the plate with airway organoid media
2 and minced with blade. The minced tissue was digested with digestion buffer (media +
3 collagenase + Dispase + ROCK inhibitor) in 37°C shaker for 30 mins. The digested
4 tissue was filtered with 100 µm filter and isolated cells were resuspended in Matrigel.
5 15-18 µl droplets of cell-Matrigel mixture was plated in 6-well plate. The cell-matrix
6 mixture was allowed to polymerize for 20-30 mins and media was added to the well.
7 The media was refreshed every 2-3 days.

8

9 **Histology and immunohistochemistry**

10 For paraffin embedded mouse lungs, mouse right ventricles were perfused with 1 ml
11 PBS and the lungs were inflated with 4% PFA, and then fixed in 4% PFA overnight at
12 4°C. After fixation, the lungs were washed by cold PBS X 4 times in 2 hrs at 4°C and
13 dehydrated in a series of increasing ethanol concentration washes (30%, 50%, 70%,
14 95% and 100%). The dehydrated lungs were incubated with Xylene for 1 hr at RT and
15 with paraffin at 65°C for 90 min X 2 times, and then embedded in paraffin and
16 sectioned. Mouse PCLS samples were fixed in 4% PFA for 30 mins. After PBS washes,
17 slices were embedded in OCT after 30% sucrose incubations. 5-8 µm thick cryosections
18 were used for immunohistochemistry. Following antibodies were used: GFP (1:400,
19 Abcam, ab6673), GFP (1:200, Abcam, ab13970), DsRed (1:200, Takara, 632496),
20 tdTomato (Sicgen, 1:200, AB8181-200), RFP (Rockland, Rockland, 600-901-379),
21 Laminin (Sigma, 1:200, L9393), S100A14 (Proteintech, 1:200, 10489-1-AP), Alpha
22 smooth muscle actin (1:200, Abcam, ab5694), PI16 (R&D systems, AF4929), LY6A

1 (R&D systems, 2 µg/ml, AF1226), APOE (1:200, Invitrogen, 701241), E-Cadherin
2 (1:200, Cell signaling, 3195S), Phospho-Histone H2A.X (1:200, Cell signaling, 9718S)
3 Human lung specimens were fixed and processed as the mouse lungs. Antibodies used
4 for human lung slide staining were ACTA2 (1:200, Abcam, ab5694), p16INK4a (1:200,
5 Santa Cruz, sc-56330), APOE (1:200, Invitrogen, 701241), FAP (1:200, R&D systems,
6 AF3715). Images were captured using Zeiss Imager M1 or Leica Stellaris 5.
7 For organoids, the Matrigel containing organoids was fixed with 4% paraformaldehyde
8 for overnight at 4°C. After multiple washes with PBS, the Matrigel was embedded in
9 OCT for cryoblock.

10

11 **Neutral lipid droplet staining**

12 Cryosections were used for the lipid staining with Bodipy 493/503 (Invitrogen, D3922). A
13 0.1% saponin-PBS solution was used for all the incubation buffers, including those for
14 blocking and antibody staining. After secondary antibody staining, the sections were
15 treated with 2.5 µM of Bodipy 493/503 for 30 mins at room temperature. Following PBS
16 washes and DAPI staining, the slides were mounted and imaged.

17

18 **Organoid analysis**

19 To obtain single cell suspensions from organoids, Matrigel containing organoids was
20 digested with Dispase (15 U/ml, Thermo Fisher Scientific) and Dnase (50 U/ml, Sigma-
21 Aldrich) for 30 mins at 37°C. Following the removal of Matrigel with Dispase, the
22 samples were washed with PBS and treated with Triple (Gibco, 12604013) for 10 mins

1 at 37°C to get single cells. The acquired single cells were then processed for FACS to
2 get EpCAM+ LUAD cells or EpCAM- fibroblasts as described above.

3

4 **Cell Culture**

5 Freshly isolated fibroblasts from KPTI lungs (GFP- or GFP+) or human lung fibroblasts
6 were cultured in DMEM/F-12 (Thermo Fisher, 11330032) with 10% FBS and 1%
7 Pen/Strep. The medium was changed every 2 days and lung fibroblasts were
8 maintained for no more than 3 passages.

9

10 **CellTrace Far Red labeling (CTFR)**

11 To compare proliferative capacity of fibroblasts, we utilized CellTrace Far Red cell
12 labeling reagent (Invitrogen, C34572). Isolated fibroblasts were cultured for 3 days and
13 then stained with CellTrace Far Red reagent. The fibroblasts were detached and
14 stained with 1 µM of CellTrace for 20 minutes at 37°C (1 million cells per ml) following
15 the manufacturer's protocol. Post staining, the cells were washed with media and
16 cultured for an additional 3 to 4 days. Serum-starved cells post-CTFR staining were
17 used to separate CTFR high and low cells based on CTFR intensity levels. CTFR high
18 cells, representing non-proliferating cells, were identified within the high intensity range
19 of 95 to 97% encompassing serum-starve cells, while cells with lower intensity were
20 considered as CTFR low cells.

21

22 **Quantitative RT-PCR (qPCR)**

1 Total RNA was obtained from cells using PicoPure RNA Isolation Kit (Applied
2 Biosystems, KIT0204) or RNeasy mini kit (QIAGEN, 74106), following the
3 manufacturers' protocols. cDNA was synthesized from total RNA using the SuperScript
4 Strand Synthesis System (Thermo Fisher, 18080044). Quantitative RT-PCR (qRT-PCR)
5 was performed using the SYBR Green system (Thermo Fisher, F415L). Relative gene
6 expression levels after qRT-PCR were defined using the $\Delta\Delta C_t$ method and normalizing
7 to the housekeeping genes. The qRT-PCR primers used for mouse are as follows:
8 Cthrc1-F: CAGTTGTCCGCACCGATCA; Cthrc1-R: GGTCCTTGTAGACACATTCCATT;
9 Acta2-F: ACTCTCTTCCAGCCATCTTTCA; Acta2-R: ATAGGTGGTTTCGTGGATGC;
10 Postn-F: TGGTATCAAGGTGCTATCTGCG; Postn-R: AATGCCAGCGTGCCATAA;
11 Tagln-F: GGTGGCTCAATTCTTGAAGGC; Tagln-R: TGCTCCTGGGCTTTCTTCATA;
12 p16INK4a-F: AATCTCCGCGAGGAAAGC; p16INK4a-R: GTCTGCAGCGGACTCCAT;
13 Myl9-F: ACAGCGCCGAGGACTTTTC; Myl9-R: AGACATTGGACGTAGCCCTCT;
14 Tpm2-F: GTGGCTGAGAGTAAATGTGGG; Tpm2-R: TTGGTGAATACTTGTCCGCT
15 Col12a1-F: AAGTTGACCCACCTTCCGAC; Col12a1-R:
16 GGTCCACTGTTATTCTGTAACCC; Apoe-F: CTGACAGGATGCCTAGCCG; Apoe-R:
17 CGCAGGTAATCCCAGAAGC; Ly6a-F: AGGAGGCAGCAGTTATTGTGG; Ly6a-R:
18 CGTTGACCTTAGTACCCAGGA; Tigit-F: TGCCTTCCTCGCTACAGG; Tigit-R:
19 TGCAGAGATGTTCTCTTTGTATC; Nkx2-1-F: CAGGACACCATGCGGAACAGC;
20 Nkx2-1-R: GCCATGTTCTTGCTCACGTCCC; Sftpc-F:
21 ATGGACATGAGTAGCAAAGAGGT; Sftpc-R: CACGATGAGAAGGCGTTTGAG;
22 Gapdh-F: GGCCCCTCCTGTTATTATGGGGGT; Gapdh-R:
23 CCCCAGCAAGGACACTGAGCAAGA

1 The primers used for human are as follows: p16INK4a-F:
2 GTCGGGTAGAGGAGGTGCG; p16INK4a-R: CATGACCTGGATCGGCCTC; p21-F:
3 TTGTACCCTTGTGCCTCGCT; p21-R: CGTTTGGAGTGGTAGAAATCTGTC;
4 CTHRC1-F: GTGGCTCACTTCGGCTAAAAT; CTHRC1-R:
5 CACTAATCCAGCACCAATTCCTT; POSTN-F: CTCATAGTCGTATCAGGGGTGCG;
6 POSTN-R: ACACAGTCGTTTTCTGTCCAC; ACTA2-F:
7 AAAAGACAGCTACGTGGGTGA; TIMP1-F: CTTCTGCAATTCCGACCTCGT; TIMP1-
8 R: ACGCTGGTATAAGGTGGTCTG; APOE-F: GTTGCTGGTCACATTCCTGG; APOE-
9 R: GCAGGTAATCCCAAAGCGAC; RPL19-F: CCCATCTTTGATGAGCTTCC; RPL19-
10 R: TGCTCAGGCTTCAGAAGAGG.

11

12 **Generation of precision-cut lung slices (PCLS) culture**

13 For mouse PCLS, lung tissues were collected 8-10 weeks after LUAD induction in KPTI
14 mouse. The lungs were perfused with PBS through the right ventricle and inflated with 1
15 to 2 ml of 2% agarose (Thermo Fisher, 16550100) dissolved in PBS by trachea. Lungs
16 were dissected from the chest cavity and submerged in ice-cold PBS to solidify
17 agarose. Lung lobes were sliced at a width of 500 μ m using a vibratome (Leica, VT
18 1000S). The slices were cultured in DMEM/F-12 (Thermo Fisher, 11330032) with 1%
19 Pen/Strep under standard cell culture conditions (37C, 5% CO₂). ABT263 (2.5 μ M),
20 ABT737 (2 μ M), Fisetin (10 μ M), DQ (1 μ M + 20 μ M), and XL888 (1 μ M) were treated
21 during the culture. At day 5, cultured PCLSs were processed for downstream analyses.

22

23 **Flow cytometry analysis of mouse PCLS**

1 The lung slices were placed into 15 ml conical tubes containing 1 ml of digestion
2 cocktail of Dispase (3 U/ml, Thermo Fisher) and Dnase (50 U/ml, Sigma) after PBS
3 washes. The slices were incubated in a digestion cocktail for 30 mins at 37°C with
4 continuous shaking. The mixture was then washed with a FACS buffer (2% FBS and
5 1% Penicillin-Streptomycin in DMEM). The mixture was passed through a 70 µm cell
6 strainer. Cells were stained with antibodies and analyzed by flow cytometry as
7 described above.

8

9 **Micro-computed tomography (CT) data acquisition and analysis**

10 An microCT system built for *in vivo* small animal imaging (U-CT, MILabs, Houten, The
11 Netherlands) was used to measure in tumor volumes *in vivo*. During the scans, animals
12 were maintained under anesthesia using approximately 2% isoflurane mixed with
13 medical grade oxygen while a total of 1,440 projects were acquired over 360° with an x-
14 ray tube voltage of 60 kVp and current of 0.24 mA. The projection data were acquired in
15 a step-and-shoot mode with x-ray exposure time of 75 ms at each step, and there were
16 two exposures at each step. No data binning was applied during the acquisition (i.e.,
17 1×1 binning). Image reconstruction was performed using the vendor-provided
18 conebeam filtered backprojection algorithm. The reconstructed image volumes were in
19 the voxel size of 0.04 mm × 0.04 mm × 0.04 mm. The volumetric matrix sizes were
20 dependent on the field of view selected during the reconstruction step focusing the
21 lungs. The reconstructed CT images were imported to the software ITK-SNAP for lung
22 tumor volume segmentation and measurement.

23

1 **Lentivirus infection**

2 Primary human lung fibroblasts or mouse lung fibroblasts were seeded and infected the
3 following day with Lenti-tTS/rtTA, Lenti-TRE-p16INK4a-T2A-dTomato, or Lenti-shApoE
4 (CCTGAACCGCTTCTGGGATTACTCGAGTAATCCCAGAAGCGGTTTCAGG). On day
5 1, the fibroblasts were infected with lentivirus at 5 multiplicity of infection (MOI) in
6 DMEM-F12 with 10% FBS and polybrene at 5 µg/ml. On day 2, cells were washed with
7 4 times with PBS and then placed in regular media (DMEM-F12, 10%FBS, 1% PS).
8 Doxycycline (1 µg/ml) treatment began 72 to 96 hours later for Lenti-tTS/rtTA and Lenti-
9 TRE-p16 dual-transduced cells.

10

11 **Fatty acid uptake analysis**

12 We used BODIPY™ 500/510 C₁, C₁₂ (D3823) to assess the transfer of fatty acid into
13 tumor organoids. After a two-week culture period, organoids were incubated overnight
14 with 2 µg/ml of BODIPY-fatty acid. Following incubation, the Matrigel and organoids
15 were dissociated to obtain single-cell suspensions. These single-cell suspensions were
16 analyzed by flow cytometry, and BODIPY fluorescence intensity was measured to
17 compare fatty acid transfer.

18

19 **Free fatty acid panel analysis**

20 A pellet of approximately 200,000 cells were homogenized into 200uL of 10% methanol
21 in water. A mix of deuterated fatty acids were spiked into 100uL of cell homogenate.
22 Samples were extracted using methanol and isoctane then derivatized using PFBB as
23 previously described³⁷. Samples were analyzed by GC-MS on an Agilent 6890N gas

1 chromatograph equipped with an Agilent 7683 autosampler. Fatty acids were separated
2 using a 15m ZB-1 column (Phenomenex) and monitored using SIM identification.
3 Analysis was performed using MassHunter software.

4

5 **Survival analysis in TCGA LUAD**

6 For survival analysis in TCGA LUADs, we utilized the web-based SurvivalGenie to
7 generate the Kaplan-Meier plot³⁸. The highly expressed genes from human
8 CDKN2A+FAP+SMA+ cluster (Supplementary Table 9) were used as input. Patient
9 tumors were categorized into high and low expression groups based on the median
10 expression levels of these genes.

11

12 **Quantification and statistical analysis**

13 GraphPad Prism was used for all statistical analyses. Statistical significance was
14 determined by ordinary one-way ANOVA or a Student's two-tailed unpaired t-test. For
15 consistency in these comparisons, the following denotes significance in all figures: * $P <$
16 0.05, ** $P <$ 0.01, *** $P <$ 0.001, **** $P <$ 0.0001.

17

18 **Data availability**

19 Previously published human scRNA-seq data that are re-analyzed in this study are
20 available in NCBI Gene Expression Omnibus (GEO) under the accession number
21 GSE183219. The sequencing data of the mouse that support the findings of this study
22 have been deposited in the accession number GSE268478.

23

1 **Code availability**

2 No custom codes were developed and used in this manuscript. All codes are available
3 by request to the corresponding author.

4

5

6

7

8

9

10

11

12

13

14

15

16

17

18

19

20

21

22

23

References

1. Campisi, J. (2013). Aging, cellular senescence, and cancer. *Annu Rev Physiol* 75, 685-705. [10.1146/annurev-physiol-030212-183653](https://doi.org/10.1146/annurev-physiol-030212-183653).
2. Krtolica, A., Parrinello, S., Lockett, S., Desprez, P.Y., and Campisi, J. (2001). Senescent fibroblasts promote epithelial cell growth and tumorigenesis: a link between cancer and aging. *Proc Natl Acad Sci U S A* 98, 12072-12077. [10.1073/pnas.211053698](https://doi.org/10.1073/pnas.211053698).
3. DuPage, M., Dooley, A.L., and Jacks, T. (2009). Conditional mouse lung cancer models using adenoviral or lentiviral delivery of Cre recombinase. *Nat Protoc* 4, 1064-1072. [10.1038/nprot.2009.95](https://doi.org/10.1038/nprot.2009.95).
4. LaFave, L.M., Kartha, V.K., Ma, S., Meli, K., Del Priore, I., Lareau, C., Naranjo, S., Westcott, P.M.K., Duarte, F.M., Sankar, V., et al. (2020). Epigenomic State Transitions Characterize Tumor Progression in Mouse Lung Adenocarcinoma. *Cancer Cell* 38, 212-228 e213. [10.1016/j.ccell.2020.06.006](https://doi.org/10.1016/j.ccell.2020.06.006).
5. Marjanovic, N.D., Hofree, M., Chan, J.E., Canner, D., Wu, K., Trakala, M., Hartmann, G.G., Smith, O.C., Kim, J.Y., Evans, K.V., et al. (2020). Emergence of a High-Plasticity Cell State during Lung Cancer Evolution. *Cancer Cell* 38, 229-246 e213. [10.1016/j.ccell.2020.06.012](https://doi.org/10.1016/j.ccell.2020.06.012).
6. Choi, J., Park, J.E., Tsagkogeorga, G., Yanagita, M., Koo, B.K., Han, N., and Lee, J.H. (2020). Inflammatory Signals Induce AT2 Cell-Derived Damage-Associated Transient Progenitors that Mediate Alveolar Regeneration. *Cell Stem Cell* 27, 366-382 e367. [10.1016/j.stem.2020.06.020](https://doi.org/10.1016/j.stem.2020.06.020).
7. Kobayashi, Y., Tata, A., Konkimalla, A., Katsura, H., Lee, R.F., Ou, J., Banovich, N.E., Kropski, J.A., and Tata, P.R. (2020). Persistence of a regeneration-associated, transitional alveolar epithelial cell state in pulmonary fibrosis. *Nat Cell Biol* 22, 934-946. [10.1038/s41556-020-0542-8](https://doi.org/10.1038/s41556-020-0542-8).
8. Strunz, M., Simon, L.M., Ansari, M., Kathiriya, J.J., Angelidis, I., Mayr, C.H., Tsidiridis, G., Lange, M., Mattner, L.F., Yee, M., et al. (2020). Alveolar regeneration through a Krt8+ transitional stem cell state that persists in human lung fibrosis. *Nat Commun* 11, 3559. [10.1038/s41467-020-17358-3](https://doi.org/10.1038/s41467-020-17358-3).
9. Reyes, N.S., Krasilnikov, M., Allen, N.C., Lee, J.Y., Hyams, B., Zhou, M., Ravishankar, S., Cassandras, M., Wang, C., Khan, I., et al. (2022). Sentinel p16(INK4a+) cells in the basement membrane form a reparative niche in the lung. *Science* 378, 192-201. [10.1126/science.abf3326](https://doi.org/10.1126/science.abf3326).
10. Elyada, E., Bolisetty, M., Laise, P., Flynn, W.F., Courtois, E.T., Burkhart, R.A., Teinor, J.A., Belleau, P., Biffi, G., Lucito, M.S., et al. (2019). Cross-Species Single-Cell Analysis of Pancreatic Ductal Adenocarcinoma Reveals Antigen-Presenting Cancer-Associated Fibroblasts. *Cancer Discov* 9, 1102-1123. [10.1158/2159-8290.CD-19-0094](https://doi.org/10.1158/2159-8290.CD-19-0094).
11. Dominguez, C.X., Muller, S., Keerthivasan, S., Koeppen, H., Hung, J., Gierke, S., Breart, B., Foreman, O., Bainbridge, T.W., Castiglioni, A., et al. (2020). Single-Cell RNA Sequencing Reveals Stromal Evolution into LRRC15(+) Myofibroblasts as a Determinant of Patient Response to Cancer Immunotherapy. *Cancer Discov* 10, 232-253. [10.1158/2159-8290.CD-19-0644](https://doi.org/10.1158/2159-8290.CD-19-0644).
12. Gorgoulis, V., Adams, P.D., Alimonti, A., Bennett, D.C., Bischof, O., Bishop, C., Campisi, J., Collado, M., Evangelou, K., Ferbeyre, G., et al. (2019). Cellular Senescence: Defining a Path Forward. *Cell* 179, 813-827. [10.1016/j.cell.2019.10.005](https://doi.org/10.1016/j.cell.2019.10.005).
13. Sahai, E., Astsaturov, I., Cukierman, E., DeNardo, D.G., Egeblad, M., Evans, R.M., Fearon, D., Greten, F.R., Hingorani, S.R., Hunter, T., et al. (2020). A framework for advancing our understanding of cancer-associated fibroblasts. *Nat Rev Cancer* 20, 174-186. [10.1038/s41568-019-0238-1](https://doi.org/10.1038/s41568-019-0238-1).

- 1 14. Andreatta, M., and Carmona, S.J. (2021). UCell: Robust and scalable single-cell gene
2 signature scoring. *Comput Struct Biotechnol J* 19, 3796-3798.
3 10.1016/j.csbj.2021.06.043.
- 4 15. Browaeys, R., Saelens, W., and Saeys, Y. (2020). NicheNet: modeling intercellular
5 communication by linking ligands to target genes. *Nat Methods* 17, 159-162.
6 10.1038/s41592-019-0667-5.
- 7 16. Yang, L.G., March, Z.M., Stephenson, R.A., and Narayan, P.S. (2023). Apolipoprotein E
8 in lipid metabolism and neurodegenerative disease. *Trends Endocrinol Metab* 34, 430-
9 445. 10.1016/j.tem.2023.05.002.
- 10 17. Padanad, M.S., Konstantinidou, G., Venkateswaran, N., Melegari, M., Rindhe, S.,
11 Mitsche, M., Yang, C., Batten, K., Huffman, K.E., Liu, J., et al. (2016). Fatty Acid
12 Oxidation Mediated by Acyl-CoA Synthetase Long Chain 3 Is Required for Mutant KRAS
13 Lung Tumorigenesis. *Cell Rep* 16, 1614-1628. 10.1016/j.celrep.2016.07.009.
- 14 18. Koundouros, N., and Poulgiannis, G. (2020). Reprogramming of fatty acid metabolism
15 in cancer. *Br J Cancer* 122, 4-22. 10.1038/s41416-019-0650-z.
- 16 19. Buechler, M.B., Pradhan, R.N., Krishnamurty, A.T., Cox, C., Calviello, A.K., Wang, A.W.,
17 Yang, Y.A., Tam, L., Caothien, R., Roose-Girma, M., et al. (2021). Cross-tissue
18 organization of the fibroblast lineage. *Nature* 593, 575-579. 10.1038/s41586-021-03549-
19 5.
- 20 20. Lee, J.Y., Reyes, N.S., Ravishankar, S., Zhou, M., Krasilnikov, M., Ringler, C., Pohan,
21 G., Wilson, C., Ang, K.K., Wolters, P.J., et al. (2024). An in vivo screening platform
22 identifies senolytic compounds that target p16INK4a+ fibroblasts in lung fibrosis. *J Clin*
23 *Invest* 134. 10.1172/JCI173371.
- 24 21. Zhu, Y., Tchkonja, T., Fuhrmann-Stroissnigg, H., Dai, H.M., Ling, Y.Y., Stout, M.B.,
25 Pirtskhalava, T., Giorgadze, N., Johnson, K.O., Giles, C.B., et al. (2016). Identification of
26 a novel senolytic agent, navitoclax, targeting the Bcl-2 family of anti-apoptotic factors.
27 *Aging Cell* 15, 428-435. 10.1111/acer.12445.
- 28 22. Zhu, Y., Tchkonja, T., Pirtskhalava, T., Gower, A.C., Ding, H., Giorgadze, N., Palmer,
29 A.K., Ikeno, Y., Hubbard, G.B., Lenburg, M., et al. (2015). The Achilles' heel of
30 senescent cells: from transcriptome to senolytic drugs. *Aging Cell* 14, 644-658.
31 10.1111/acer.12344.
- 32 23. Grout, J.A., Sirven, P., Leader, A.M., Maskey, S., Hector, E., Puisieux, I., Steffan, F.,
33 Cheng, E., Tung, N., Maurin, M., et al. (2022). Spatial Positioning and Matrix Programs
34 of Cancer-Associated Fibroblasts Promote T-cell Exclusion in Human Lung Tumors.
35 *Cancer Discov* 12, 2606-2625. 10.1158/2159-8290.CD-21-1714.
- 36 24. Han, G., Sinjab, A., Rahal, Z., Lynch, A.M., Treekitkarnmongkol, W., Liu, Y., Serrano,
37 A.G., Feng, J., Liang, K., Khan, K., et al. (2024). An atlas of epithelial cell states and
38 plasticity in lung adenocarcinoma. *Nature* 627, 656-663. 10.1038/s41586-024-07113-9.
- 39 25. Hayflick, L., and Moorhead, P.S. (1961). The serial cultivation of human diploid cell
40 strains. *Exp Cell Res* 25, 585-621. 10.1016/0014-4827(61)90192-6.
- 41 26. Dost, A.F.M., Moye, A.L., Vedaie, M., Tran, L.M., Fung, E., Heinze, D., Villacorta-Martin,
42 C., Huang, J., Hekman, R., Kwan, J.H., et al. (2020). Organoids Model Transcriptional
43 Hallmarks of Oncogenic KRAS Activation in Lung Epithelial Progenitor Cells. *Cell Stem*
44 *Cell* 27, 663-678 e668. 10.1016/j.stem.2020.07.022.
- 45 27. Chen, P.H., Cai, L., Huffman, K., Yang, C., Kim, J., Faubert, B., Boroughs, L., Ko, B.,
46 Sudderth, J., McMillan, E.A., et al. (2019). Metabolic Diversity in Human Non-Small Cell
47 Lung Cancer Cells. *Mol Cell* 76, 838-851 e835. 10.1016/j.molcel.2019.08.028.
- 48 28. Gouw, A.M., Eberlin, L.S., Margulis, K., Sullivan, D.K., Toal, G.G., Tong, L., Zare, R.N.,
49 and Felsher, D.W. (2017). Oncogene KRAS activates fatty acid synthase, resulting in
50 specific ERK and lipid signatures associated with lung adenocarcinoma. *Proc Natl Acad*
51 *Sci U S A* 114, 4300-4305. 10.1073/pnas.1617709114.

- 1 29. Jackson, E.L., Willis, N., Mercer, K., Bronson, R.T., Crowley, D., Montoya, R., Jacks, T.,
2 and Tuveson, D.A. (2001). Analysis of lung tumor initiation and progression using
3 conditional expression of oncogenic K-ras. *Genes & development* 15, 3243-3248.
- 4 30. Jackson, E.L., Olive, K.P., Tuveson, D.A., Bronson, R., Crowley, D., Brown, M., and
5 Jacks, T. (2005). The differential effects of mutant p53 alleles on advanced murine lung
6 cancer. *Cancer research* 65, 10280-10288.
- 7 31. Madisen, L., Zwingman, T.A., Sunkin, S.M., Oh, S.W., Zariwala, H.A., Gu, H., Ng, L.L.,
8 Palmiter, R.D., Hawrylycz, M.J., and Jones, A.R. (2010). A robust and high-throughput
9 Cre reporting and characterization system for the whole mouse brain. *Nature*
10 *neuroscience* 13, 133-140.
- 11 32. Reyes, N.S., Krasilnikov, M., Allen, N.C., Lee, J.Y., Hyams, B., Zhou, M., Ravishankar,
12 S., Cassandras, M., Wang, C., and Khan, I. (2022). Sentinel p16 INK4a+ cells in the
13 basement membrane form a reparative niche in the lung. *Science* 378, 192-201.
- 14 33. DuPage, M., Dooley, A.L., and Jacks, T. (2009). Conditional mouse lung cancer models
15 using adenoviral or lentiviral delivery of Cre recombinase. *Nature protocols* 4, 1064-
16 1072.
- 17 34. Lee, J.Y., Reyes, N.S., Ravishankar, S., Zhou, M., Krasilnikov, M., Ringler, C., Pohan,
18 G., Wilson, C., Ang, K.K.-H., and Wolters, P.J. (2024). An in vivo screening platform
19 identifies senolytic compounds that target p16 INK4a+ fibroblasts in lung fibrosis. *The*
20 *Journal of Clinical Investigation*.
- 21 35. Janesick, A., Shelansky, R., Gottscho, A.D., Wagner, F., Williams, S.R., Rouault, M.,
22 Beliakoff, G., Morrison, C.A., Oliveira, M.F., and Sichertman, J.T. (2023). High resolution
23 mapping of the tumor microenvironment using integrated single-cell, spatial and in situ
24 analysis. *Nature Communications* 14, 8353.
- 25 36. Sachs, N., Papaspyropoulos, A., Zomer-van Ommen, D.D., Heo, I., Böttinger, L., Klay,
26 D., Weeber, F., Huelsz-Prince, G., Iakobachvili, N., and Amatngalim, G.D. (2019). Long-
27 term expanding human airway organoids for disease modeling. *The EMBO journal* 38,
28 e100300.
- 29 37. Quehenberger, O., Armando, A.M., and Dennis, E.A. (2011). High sensitivity quantitative
30 lipidomics analysis of fatty acids in biological samples by gas chromatography–mass
31 spectrometry. *Biochimica et Biophysica Acta (BBA)-Molecular and Cell Biology of Lipids*
32 1811, 648-656.
- 33 38. Dwivedi, B., Mumme, H., Satpathy, S., Bhasin, S.S., and Bhasin, M. (2022). Survival
34 Genie, a web platform for survival analysis across pediatric and adult cancers. *Scientific*
35 *Reports* 12, 3069.
- 36
37
38
39
40
41
42
43
44
45
46

1 **Figure legends**

2 **Figure 1. Contribution of senescent $p16^{Ink4a+}$ fibroblasts to CAFs in mouse LUAD.**

3 (A) Schematic of experimental design to investigate $p16^{Ink4a+}$ fibroblasts in mouse
4 LUAD and demonstration of capacity to sort for $p16^{Ink4a+}$ fibroblasts from LUAD tissues.

5 (B) Representative immunofluorescence images showing nuclear GFP+ cells (green)
6 within the stroma (Laminin+, red) in the lungs of KPTI mice at 8-10 weeks post-tumor
7 induction. Scale bars, 200 μ m.

8 (C) Representative image of immunostaining of GFP, ACTA2, PI16, and tdTomato in
9 the lungs of KPTI mice at 10 weeks post-tumor induction. Scale bars, 50 μ m.

10 (D) Top: UMAP plot of scRNA-seq data from fibroblasts isolated from KPTI and normal
11 mouse lungs. Bottom: Proportion of fibroblast subtype relative to the total fibroblast
12 population within each condition.

13 (E) Left: Representative image of immunostaining for γ H2AX and F-Actin in $p16^{Ink4a-}$
14 and $p16^{Ink4a+}$ fibroblasts isolated from KPTI mouse lungs. Right: Quantitative analysis of
15 γ H2AX+ cells (n=18 per group). Scale bars, 50 μ m.

16 (F) Spatial profiling of mouse LUAD section using Xenium In Situ to elucidate the
17 distribution of $p16^{Ink4a+}$ fibroblasts expressing CAF markers within LUAD tissue. Each
18 colored dots represents transcript detection overlaid on segmented cell borders.
19 Tumor/stroma defined by presence/absence of tumor and stromal-specific transcripts.

20 (G) Gene expression density map of iCAF/adventitial and myCAF markers relative to
21 the tumor margins.

22 Unpaired *t*-test was used in (E) to test statistical significance. Data are represented as
23 mean \pm SD.; ****P* < 0.001

1

2 **Figure 2. $p16^{Ink4a+}$ CAFs promote LUAD progression by supporting adjacent**
3 **HPCS cells.**

4 (A) UMAP derived from spatially analyzed transcripts from KPTI mouse lung section.

5 (B) Gene Density of HPCS and AT2 markers within the tumor.

6 (C) ImageDimPlot of KPTI mouse lung with cell positions annotated by cluster labels,
7 with localization of AT2, HPCS, and myCAF clusters in the region of interest. Scale
8 bars, 500 μm .

9 (D) Transcript mapping with cell segmentation highlighting the proximity between
10 $p16^{Ink4a+}$ myCAFs and S100a14+ HPCS cells. Scale bars, 50 μm .

11 (E) S100a14 transcript localization aligned with H&E of KPTI lungs with tumor histologic
12 grading for aggressive features. Scale bars, 1000 μm .

13 (F) Immunofluorescence identification of GFP+ACTA2+ fibroblasts (indicated by green
14 arrowheads) and S100A14+tdTomato+ HPCS cells (indicated by yellow arrowheads) in
15 KPTI mouse LUAD. Scale bars, 100 μm .

16 (G) Quantification of the distance between GFP+ACTA2+ fibroblasts and S100A14+ or
17 S100A14- tumor cells, with individual measurements represented as data points (n=103
18 for S100A14-, n=115 for S100A14+).

19 Unpaired *t*-test was used in (G) to test statistical significance. Data are represented as
20 mean \pm SD.; **P* < 0.05, ****P* < 0.001, *****P* < 0.0001

21

22 **Figure 3. $p16^{Ink4a+}$ fibroblasts support LUAD growth by increasing HPCS cells *in***
23 ***vitro* and *in vivo*.**

- 1 (A) Top: Schematic of the co-culture setup of FACS-sorted fibroblasts and tdTomato+
- 2 LUAD cells under air-liquid interface conditions. Bottom: Images of 3D tumor organoids.
- 3 (B) Quantitative analysis of organoid sizes established in (A).
- 4 (C) Representative images of LY6A immunofluorescence in organoids formed as
- 5 described in (A). Scale bars, 100 μm .
- 6 (D) Flow cytometry analysis of LY6A+ cell populations in 3D tumor organoids.
- 7 (E) Single-cell RNA sequencing of tdTomato+ cells from organoids established in (A).
- 8 Left: Unsupervised clustering of scRNA-seq data, annotated based on Marjanovic et al.
- 9 Right: UMAP plot showing distinct cellular population that emerges in the tumor
- 10 organoids co-cultured with p16^{Ink4a+} fibroblasts.
- 11 (F) Pie graph depicting the proportion of cells contributing to identified clusters.
- 12 (G) Top: Outline of the *in vivo* transplantation of tdTomato+ LUAD cells with either
- 13 p16^{Ink4a+} or p16^{Ink4a-} fibroblasts into NSG mice. Bottom: microCT images of mouse lungs
- 14 4 weeks post-transplantation, Scale bars, 1 cm.
- 15 (H) Tumor burden quantification in transplanted mice, expressed as tumor volume
- 16 relative to whole lung volume at 4 weeks post-transplantation.
- 17 (I) Representative image of S100A14 and LY6A immunofluorescence in the lungs of
- 18 recipient mice, 4 weeks post-transplantation. Scale bars, 100 μm .
- 19 (J) Quantitative analysis of HPCS cell prevalence within tdTomato+ tumor lesions.
- 20 Unpaired *t*-test was used in (B), (D), (H), (J) to test statistical significance. Data are
- 21 represented as mean \pm SD.; **P* < 0.05, ****P* < 0.001, *****P* < 0.0001
- 22

1 **Figure 4. APOE derived from p16^{Ink4a+} fibroblasts promotes LUAD expansion by**
2 **enriching the HPCS population.**

3 (A) NicheNet analysis of ligand-receptor interactions between p16^{Ink4a+} fibroblasts and
4 tdTomato+ LUAD cells from KPTI mouse lungs.

5 (B) Representative image of APOE immunofluorescence in KPTI lung tissue, indicating
6 high expression of APOE in GFP+ACTA2+ fibroblasts.

7 (C) qPCR evaluation of Apoe expression in fibroblasts sorted from KPTI mouse lungs.
8 Each data point represents a separate biological replicate.

9 (D) Xenium in situ visualization of Postn, Apoe, and GFP expression patterns within
10 tumor areas in KPTI mouse lung.

11 (E) Images of 3D tumor organoids treated with recombinant mouse APOE (rmAPOE).
12 (F) Assessment of tumor organoid sizes with rmAPOE treatment.

13 (G) Immunofluorescence detection of LY6A in tumor organoids derived from the
14 experiment in (E). Scale bars, 100 μ m.

15 (H) Determination of LY6A+ cell percentages in organoids via flow cytometry.

16 (I) Representative image of 3D tumor organoids treated with COG133, an ApoE mimetic
17 peptide, to observe inhibitory effects on p16^{Ink4a+} fibroblasts function.

18 (J) Measurement of sizes of tumor organoids established in (H).

19 (K) Flow cytometry-based quantification of LY6A+ cells in tumor organoids treated with
20 COG133.

21 Unpaired *t*-test was used in (C), (F), (H), (J), and (K) to test statistical significance. Data
22 are represented as mean \pm SD.; **P* < 0.05, ****P* < 0.001, *****P* < 0.0001
23

1 **Figure 5. APOE from p16^{Ink4a+} fibroblasts modulates lipid metabolism in LUAD.**
2 (A) Left: Oil Red O staining of KPTI mouse lung tissue for lipid deposits. Scale bars, 100
3 μm . Right: LY6A immunofluorescence coupled with Bodipy 493/503 staining for neutral
4 lipids in KPTI mouse lung. Scale bars, 50 μm .
5 (B) Xenium in situ imaging aligned with H&E staining demonstrates localization of Apoe
6 and Cldn4 transcripts within vacuolized regions in KPTI lung tissue.
7 (C) Top: Schematic of 3D tumor organoid culture with treatment of rmAPOE protein.
8 Bottom: Representative images of immunofluorescence of LY6A and Bodipy 493/503
9 staining for neutral lipids in 3D tumor organoids. Scale bars, 25 μm .
10 (D) Diagram outlining the Bodipy fatty acid (Bodipy-C12) transfer assay in 3D tumor
11 organoids.
12 (E) Graph illustrating the increase in Bodipy-C12 Mean Fluorescence Intensity (MFI) in
13 tdT+ tumor cells following rmAPOE treatment, suggesting enhanced fatty acid uptake.
14 Right: MFI quantification of Bodipy-C12 in tdT+ tumor cells co-cultured with p16^{Ink4a+}
15 fibroblasts
16 (F) MFI quantification of Bodipy-C12 in tdT+ tumor cells co-cultured with p16^{Ink4a+}
17 fibroblasts; downregulation of Apoe using shRNA indicates the role of APOE in
18 supporting tumor cell fatty acid uptake.
19 (G) Heatmap showing the log₂ fold change in free fatty acid levels in tumor organoids
20 cultured with p16^{Ink4a-} fibroblasts, comparing the effects of vehicle and rmAPOE
21 treatment.

1 (H) Schematic representing the metabolism of fatty acids, including their conversion into
2 acyl-carnitines via carnitine palmitoyltransferase 1 (CPT1) for entry into fatty acid
3 oxidation pathways.

4 (I) Images of tumor organoids co-cultured with p16^{Ink4a} fibroblasts and treated with
5 either vehicle or etomoxir, a CPT1 inhibitor.

6 (J) Organoid size quantification reveals that inhibition of fatty acid oxidation disrupts the
7 tumor-supportive role of p16^{Ink4a} fibroblasts.

8 (K) Flow cytometry analysis of the LY6A⁺ cell proportion in tumor organoids subjected
9 to fatty acid oxidation inhibition.

10 One-way ANOVA was used in (E) and (F) and unpaired *t*-test was used in (J) and (K) to
11 test statistical significance. Data are represented as mean ± SD.; **P* < 0.05, ***P* < 0.01,

12 ****P* < 0.001, *****P* < 0.0001

13

14 **Figure 6. Senolytic compound XL888 clears p16^{Ink4a} fibroblasts and reduces**
15 **tumor burden in KPTI mice.**

16 (A) Generation of PCLS cultures from KPTI mouse lungs.

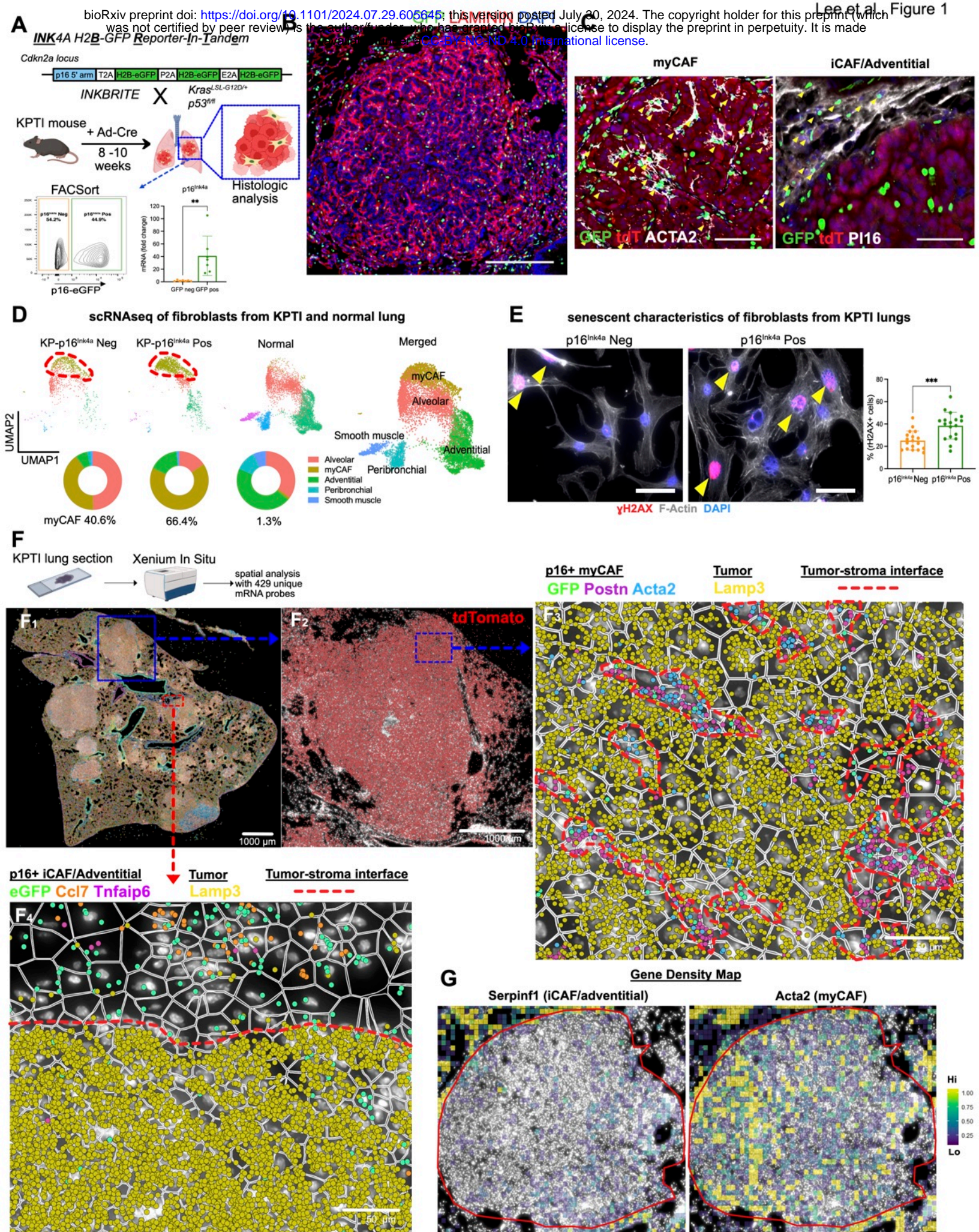
17 (B) Brightfield and fluorescence images of PCLS demonstrating the preservation of
18 tdTomato⁺ LUAD and GFP⁺ cells. Scale bars, 1000 μm.

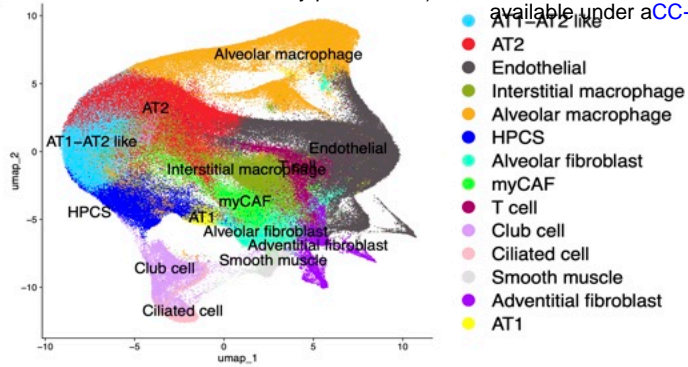
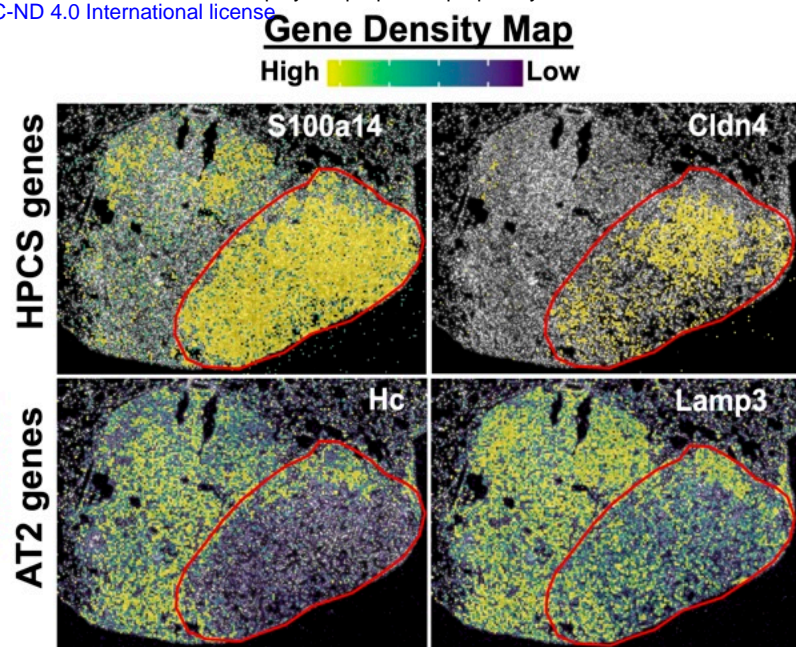
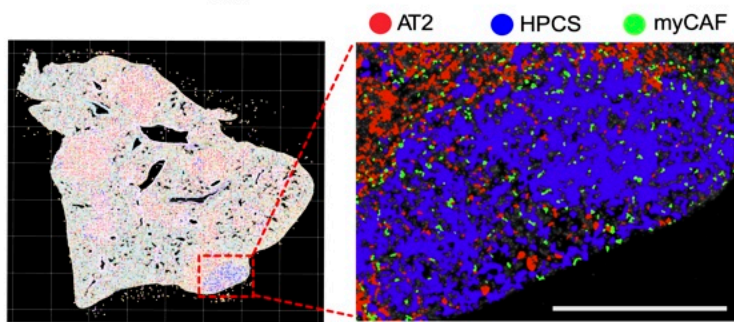
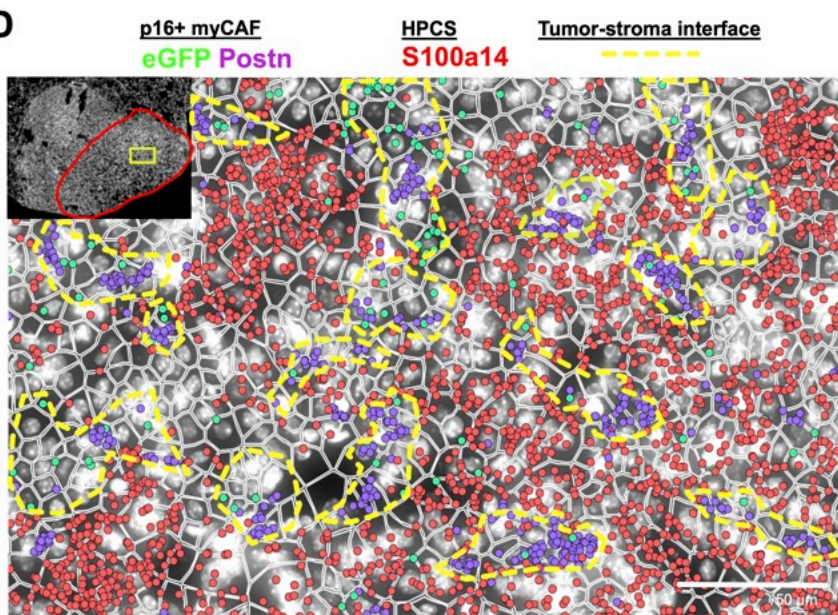
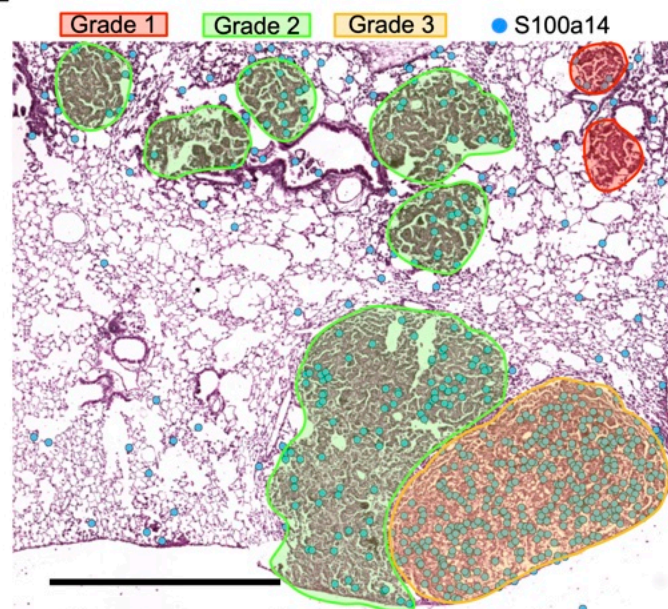
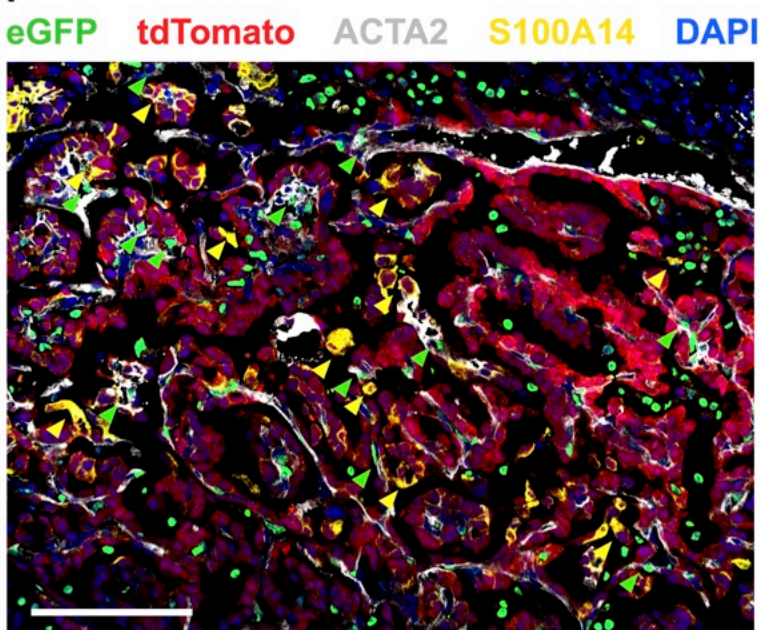
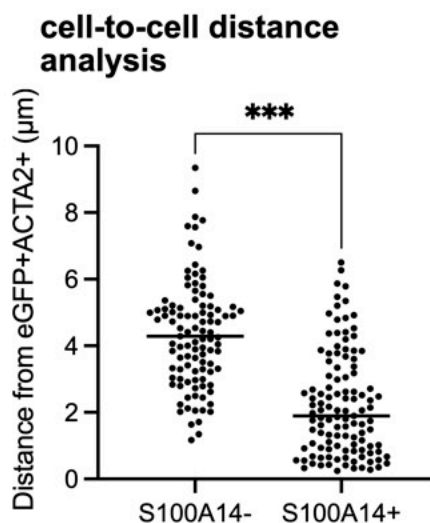
19 (C) Flow cytometry strategy for evaluating GFP⁺ cells within sorted (CD45-EpCAM-
20 CD31⁻) fibroblasts post-XL888 treatment.

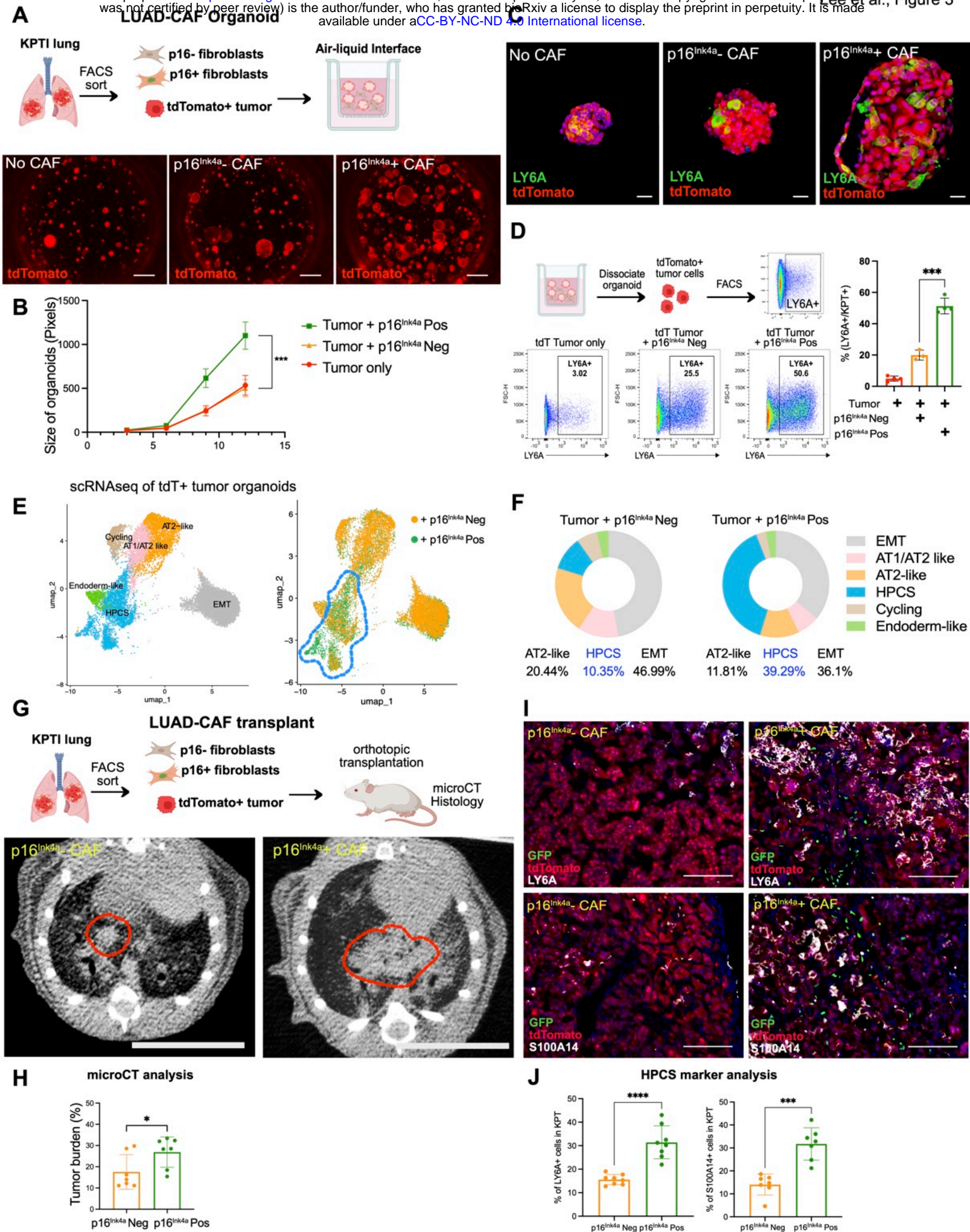
21 (D) Flow cytometry analysis of GFP⁺ fibroblasts in PCLS treated with XL888 (n=3 slices
22 for each group).

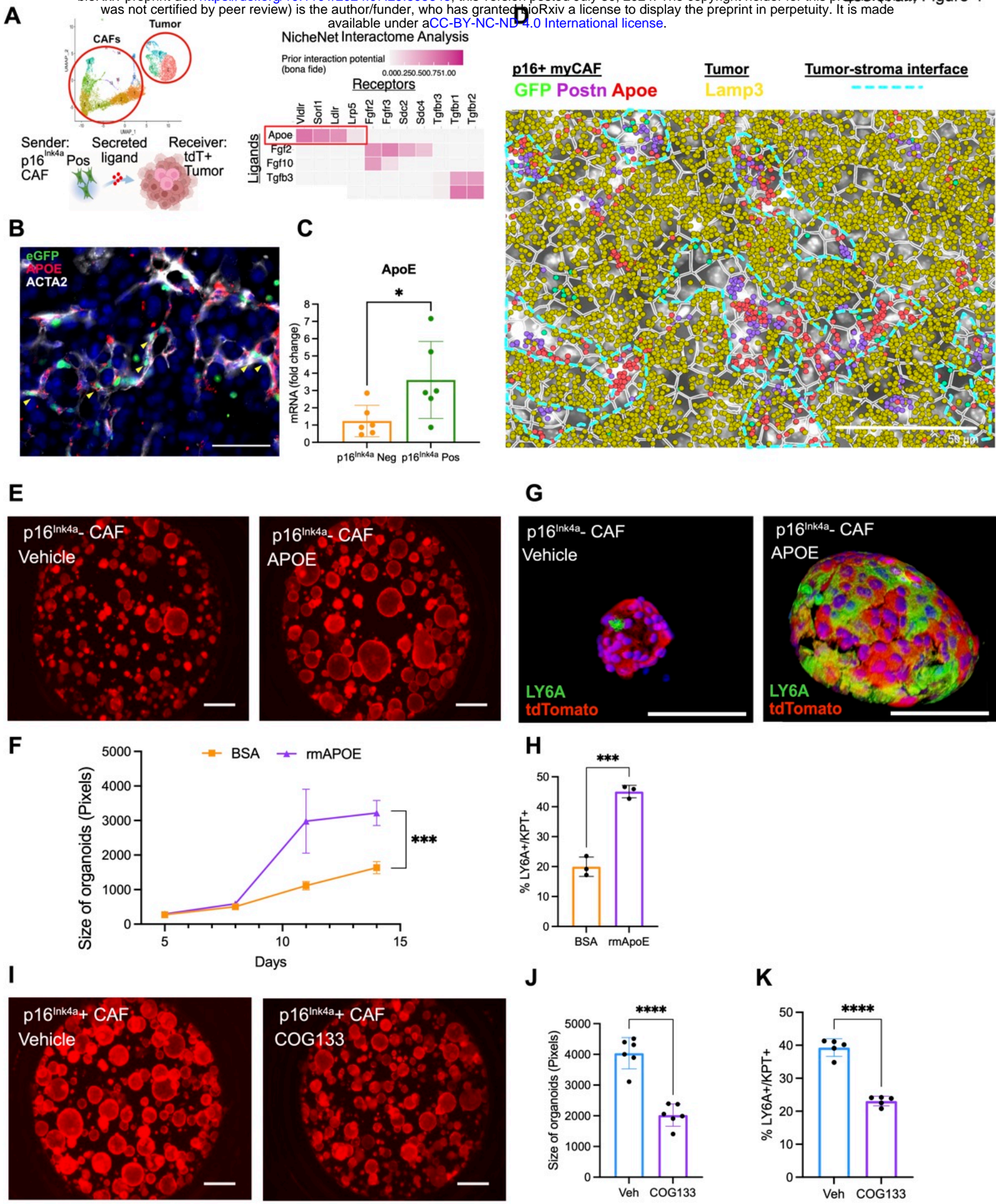
- 1 (E) Representative image of GFP and ACTA2 immunofluorescence in PCLS treated
2 with vehicle or XL888. Scale bars, 100 μ m.
- 3 (F) Quantitative analysis of GFP+ cells among ACTA2+ fibroblasts (n=10 for each
4 group).
- 5 (G) Experimental design to test tumor suppressive effect of XL888 in KPTI mouse (top),
6 alongside representative macroscopic lung images from vehicle- and XL888-treated
7 groups (bottom).
- 8 (H) MicroCT images of lungs from KPTI mice following treatment. Scale bars, 1 cm.
- 9 (I) Assessment of tumor burden in KPTI mice by microCT, expressed as the tumor
10 volume to whole lung volume ratio (n=14-15 mice for each group).
- 11 (J) Representative image of GFP and ACTA2 immunofluorescence of KPTI mouse lung
12 tissue. Scale bars, 200 μ m.
- 13 (K) Quantification of p16^{Ink4a}+ myCAFs in KPTI mouse lung (n=6-7 mice for each
14 group).
- 15 (L) Representative image of S100A14, LY6A, and tdTomato immunofluorescence of
16 KPTI lung tissue. Scale bars, 200 μ m.
- 17 (M) Quantification of the proportion of HPCS cells, identified by S100A14 (left) and
18 LY6A (right), within the tdTomato+ LUAD cell population in KPTI mouse lungs (n=6-7
19 mice for each group).
- 20 Unpaired t-test was used in (d), (f), (i), (k), and (m) to test statistical significance. Data
21 are represented as mean \pm SD.; **P < 0.01, ***P < 0.001, ****P < 0.0001
22
- 23 **Figure 7. Contribution of p16^{Ink4a}+ fibroblasts to human LUAD progression.**

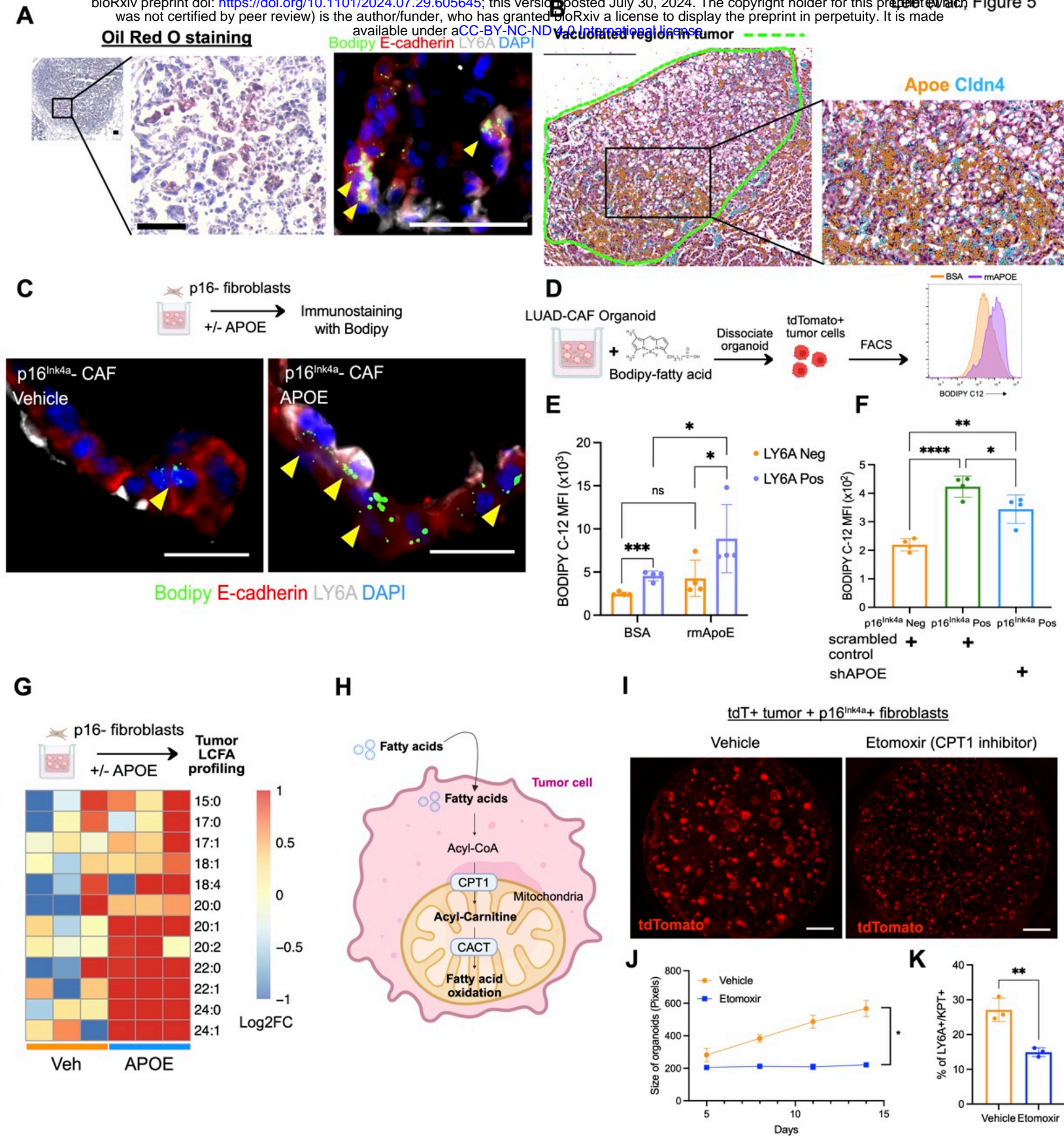
- 1 (A) UMAP derived from spatially analyzed transcripts from human LUAD section.
- 2 (B) ImageDimPlot of human LUAD section with cell positions annotated by cluster labels
- 3 (left), localization of KRT8+/CLDN4+ cells (blue), and myCAFs (yellow) with transcripts
- 4 of CDKN2A, APOE, and CLDN4 in the region of interest (right). Scale bars, 200 μ m.
- 5 (C) Survival analysis of LUAD patients in the TCGA based on expression level of gene
- 6 signature in the $p16^{INK4A+}$ CAF cluster from a human CAF single cell data set (Grout *et*
- 7 *al.*).
- 8 (D) Experimental design to test the effects of $p16^{INK4A}$ -overexpression (p16OE) in
- 9 human lung fibroblasts on human LUAD (hLUAD) organoids.
- 10 (E) Images of hLUAD organoids cultured with either control or p16OE fibroblasts. Scale
- 11 bars, 2000 μ m.
- 12 (F) Quantification of hLUAD organoids in (e) (n=5 for each group).
- 13 (G) qPCR analysis of $p16^{INK4A}$ and p21 in normal human lung fibroblasts after
- 14 overexpression of $p16^{INK4A}$ (n=3 for each group).
- 15 (H) qPCR analysis of control or p16OE lung fibroblasts with or without co-culture with
- 16 tumor (n=3 for each group).
- 17 (I) Left: Flow cytometry image of tumor organoids from (E). Right: Quantification of
- 18 Integrin $\alpha 2$ high plastic cell population within tumor organoids (n=4 for each group).
- 19 (J) Analysis of fatty acid transfer within tumor organoids established in (E) (n=3 for each
- 20 group).
- 21 Unpaired *t*-test was used in (F), (G), (I), (J) and and one-way ANOVA was used in (H) to
- 22 test statistical significance. Data are represented as mean \pm SD.; **P* < 0.05, ***P* < 0.01,
- 23 ****P* < 0.001, *****P* < 0.0001

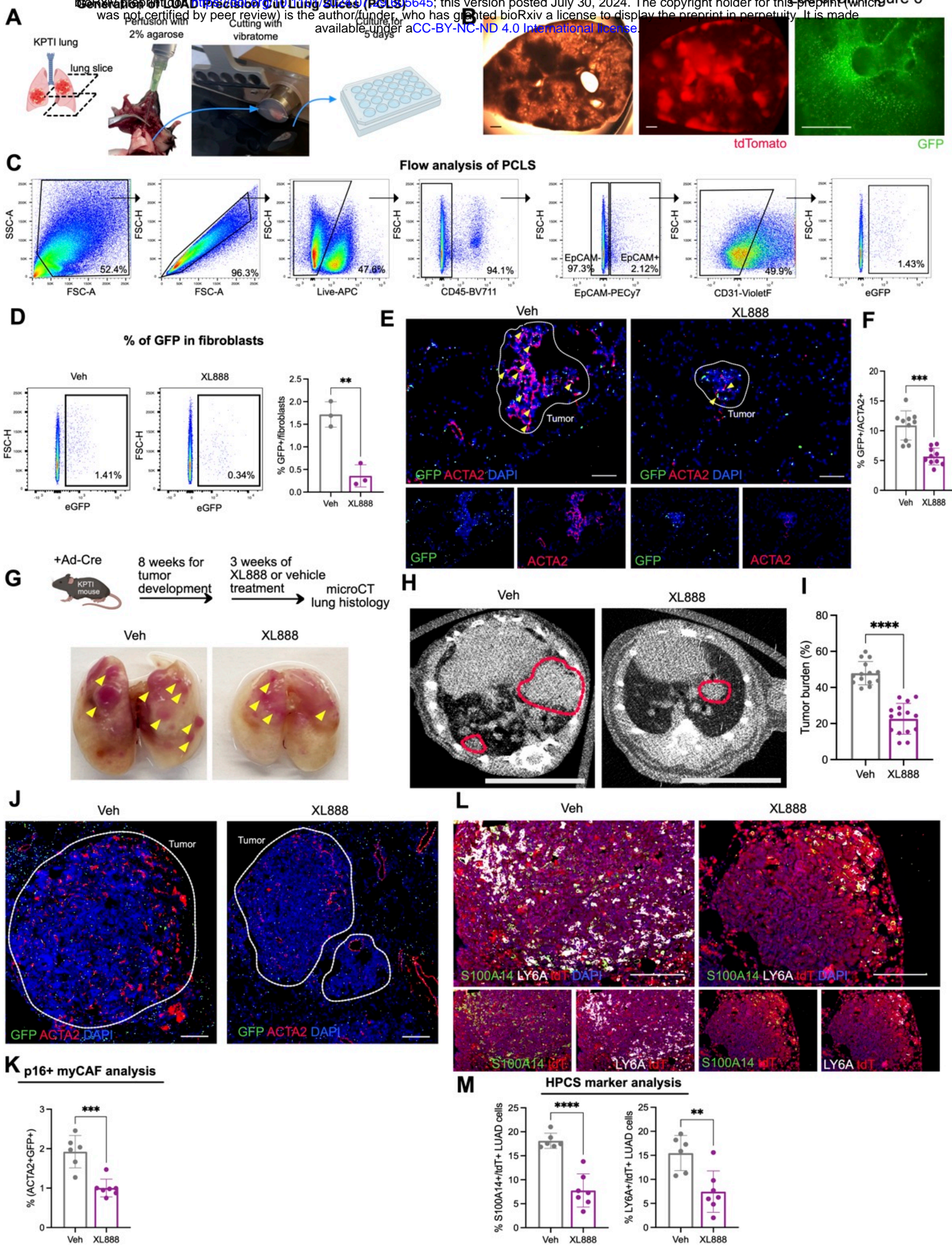


A**B****C****D****E****F****G**









Human LUAD tissue with KRAS driver mutation

myCAF KRT8+/CLDN4+

